Climatic Impacts of Stratospheric Geoengineering with Sulfate, Black Carbon and Titania Injection

Anthony C. Jones[1], James M. Haywood[1,2] and Andy Jones[2]

[1]{College of Engineering Maths and Physical Sciences, University of Exeter, Exeter, United Kingdom}

[2]{Met Office Hadley Centre, Exeter, United Kingdom}

Correspondence to: A. C. Jones (aj247@exeter.ac.uk)

Abstract

In this paper, we examine the potential climatic effects of geoengineering by sulfate, black carbon and titania injection against a baseline RCP8.5 scenario. We use the HadGEM2-CCS model to simulate scenarios in which the top-of-the-atmosphere radiative imbalance due to rising greenhouse gas concentrations is offset by sufficient aerosol injection throughout the 2020-2100 period. We find that the global-mean temperature is effectively maintained at historical levels for the entirety of the period for all 3 aerosol-injection scenarios, though there are a wide range of side-effects which are discussed in detail. The most prominent conclusion is that although the BC injection rate necessary to produce an equivalent global mean temperature-response is much lower, the severity of stratospheric temperature changes (> +70 ^{o}C) and precipitation impacts effectively exclude BC from being a viable option for geoengineering. Additionally, while it has been suggested that titania would be an effective particle because of its high scattering efficiency, it also efficiently absorbs solar ultraviolet radiation producing a significant stratospheric warming (> +20 ^{o}C). As injection rates and climatic impacts for titania are close to those for sulfate, there appears to be little benefit in terms of climatic influence of using titania when compared to the injection of sulfur dioxide, which has the added benefit of being well modelled through extensive research that has been carried out on naturally occurring explosive volcanic eruptions.

1 Introduction

The climatic impacts of continued greenhouse gas (GHG) emissions are likely to be severe which has prompted countenance of new strategies for tackling GHG-induced global warming [e.g Collins et al., 2013]. Geoengineering strategies, or large-scale climate interventions that aim to reduce global warming, include strategies to sequester atmospheric carbon dioxide – Carbon Dioxide Removal (CDR) methods, and strategies to reduce solar irradiance at Earth's surface – Solar Radiation Management (SRM) methods [Shepherd et al., 2009]. Stratospheric Aerosol Injection (SAI), an SRM scheme which has received significant attention, involves the enhancement of the stratospheric aerosol layer in order to reflect more sunlight back to space. This scheme mimics large volcanic eruptions such as Mt Pinatubo in 1991, which injected approximately 15-20 Tg of sulfur dioxide (SO_2) into the tropical stratosphere and induced a globally averaged surface cooling of around -0.3 ^{o}C for the following two years [Stenchikov et al., 2002].

Sulfate (SO_4) aerosols have featured predominantly in SAI research because of the volcanic analogue (e.g. in the Geoengineering Model Intercomparison Project, GeoMIP [Kravitz et al., 2013]). General Circulation Model (GCM) simulations suggest that, while sufficient sulfate injection could effectively reduce global-mean temperature, possible side effects include changes to regional precipitation [e.g. Bala et al., 2008; Tilmes et al., 2013], ozone [e.g. Tilmes et al., 2009; Pitari et al., 2014], stratospheric dynamics [Aquila et al., 2014] and sea-ice extent [Berdahl et al., 2014]. Precipitation changes could result from changes to the moist static stability of the atmosphere and a concomitant weakening of the hydrological cycle [Bala et al., 2008], and the regional precipitation changes under GeoMIP simulations have been shown to be reasonably consistent across a range of climate models [Tilmes et al., 2013]. Ozone concentrations could change as a result of enhanced heterogeneous chemistry on the surface of sulfate aerosols or indirectly by changes to the stratospheric dynamics and chemistry [e.g. Tilmes et al., 2009]. Stratospheric dynamical changes could occur as the result of tropical heating in the sulfate layer and by changes to wave propagation from the troposphere [e.g. Aquila et al., 2014].

In order to ameliorate the known side-effects of sulfate injection, some authors have proposed alternative aerosols to sulfate [e.g. Teller et al., 1997]. Crutzen (2006) suggested the possible injection of black carbon (BC), which would mimic hypothetical nuclear winter scenarios. One advantage of BC over sulfate is that less mass would be needed for an equivalent

radiative forcing [Crutzen, 2006]. BC particles efficiently absorb solar radiation, unlike sulfate which primarily reflects solar radiation [Ferraro et al., 2011]. Alternatively, minerals such as titania (TiO_2), silica (SiO_2) and alumina (Al_2O_3), which have a high refractive index at wavelengths of peak solar radiative flux (~550 nm), have also been suggested [Pope et al., 2012]. Although the use of alternative aerosols is not a new suggestion [e.g. Teller et al., 1997], comparatively little research has been conducted on their potential utility. Kravitz et al (2012) simulated a constant BC injection scenario of 1 Tg/yr in the tropics for small radius (0.03 μm) and large radius (0.15 μm) aerosols. They found that the small particle BC aerosol scenario produced a global surface cooling of -9.45 ^{o}C, but also induced stratospheric warming > +60 ^{o}C and global ozone loss of 50%. The large particle BC aerosol scenario had a neglible climatic impact. Using a fixed dynamical heating (FDH) code, Ferraro et al (2011) compared the stratospheric heating of sulfate, titania, and BC layers for an equivalent instantaneous radiative forcing. Their results showed a tropical stratospheric warming signal for all the aerosols, though much greater in the case of BC. To date, no work has used a comprehensive fully coupled atmosphere-ocean GCM to directly compare the possible climatic impacts of SAI with alternative aerosols to sulfate, which is the motivation for this research.

In this work, we simulate the stratospheric injection of sulfate, titania and BC against a baseline RCP8.5 concentrations scenario using a fully-coupled GCM. Titania is selected to represent an efficient light-scattering aerosol and BC is selected as a light-absorbing aerosol. RCP8.5, which is the high-end carbon-intensive CMIP5 scenario, is selected to give a significant greenhouse effect against which to employ geoengineering, in order to distinguish the climatic impacts specific to each aerosol. Observations have shown that the current global GHG emissions exceed the emissions inherent in RCP8.5 [Peters et al., 2013]; therefore our work could be considered as geoengineering against a business-as-usual scenario. Additionally, the next generation of GeoMIP simulations (GeoMIP6) will utilise a carbon-intensive scenario [Kravitz et al., 2015], hence our work will provide a useful supplement to those results. We chose to inject aerosol at a sufficient rate to counterbalance the Top Of the Atmosphere (TOA) global/annual-mean radiative flux imbalance caused by increasing atmospheric GHGs. Our simulation design is similar to the G3 scenario of the Geoengineering Model Intercomparison Project (GeoMIP), which instead used the RCP4.5 concentrations scenario as its baseline and injected sulfate at a sufficient rate to counterbalance GHG radiative forcing [Kravitz et al., 2011]. We analyse the climate changes in the 2090s with

respect to a simulated historical period and discuss impacts on a wide range of meteorological parameters.

2 Model

2.1. The HadGEM2-CCS model

For this investigation, we use the HadGEM2-CCS climate model in a fully coupled atmosphere-ocean mode. HadGEM2-CCS is the high-top configuration of the HadGEM2 family of models, and includes a well-resolved stratosphere. The atmosphere component comprises 60 vertical levels extending to 84km and a horizontal resolution of 1.25^{o} x 1.875^{o} latitude by longitude respectively. The 40-level ocean component has a horizontal resolution of 1^{o} by 1^{o} from the poles to 30^{o}N/S, with the latitudinal resolution then increasing smoothly to 0.33^{o} at the equator [The HadGEM2 Development Team, 2011]. For this investigation, GHG concentrations, stratospheric ozone, anthropogenic aerosols and aerosol precursor gases are prescribed following the Coupled Model Intercomparison Project phase 5 (CMIP5) [Taylor et al., 2012] protocol, with historical data from 1860-2005 and RCP8.5 concentrations from 2005-2100. HadGEM2-CCS contains the aerosol module Coupled Large-scale Aerosol Simulator for Studies in Climate (CLASSIC). The module's sulfur cycle is described in detail in Bellouin et al (2011). Briefly, it includes the oxidation of sulfur dioxide (SO_2) to sulfate aerosol in aqueous and gas phase reactions. Sulfate is represented by Aitken, accumulation and dissolved modes, with hygroscopic growth in the accumulation mode following d'Almeida et al (1991). Aerosol size modes are represented by lognormal size-distributions with a prescribed dry-mode median radius (r_m) and geometric standard deviation (σ).

2.2 Stratospheric aerosol microphysical and optical properties

For this investigation, stratospheric sulfate is modelled using the *volc2* size-distribution from Rasch et al (2008) for the sulfate accumulation mode, with r_m = 0.376 μm and σ = 1.25; the relatively large r_m is chosen to reflect the high concentrations of SO_2 injected in this experiment.

CLASSIC includes a tropospheric BC scheme with fresh, aged and in-cloud modes [Bellouin et al., 2011]. We introduce an additional non-hygroscopic stratospheric BC component and prescribe a lognormal size-distribution with r_m = 0.0118 μm and σ = 2.0, which is taken from

tropospheric BC observations [Deepak and Gerber, 1983]. We prescribe a density for BC of 1000 kg/m^3 and take refractive indices from a World Meteorological Organisation report [Deepak and Gerber, 1983].

For stratospheric titania, we assume the non-hygroscopic lognormal size distribution of Pope et al. (2012) with r_m = 0.045 μm and σ = 1.8. This size-distribution was selected to give the titania aerosol a high scattering efficiency, as shown by Pope et al (2012). We prescribe a density for titania of 4230 kg/m^3 [Pope et al, 2012], and for the refractive indices we follow Ferraro et al (2011) and use the average of the extra-ordinary and ordinary values from Ribarsky (1985).

The specific absorption (k_{abs}) and scattering (k_{sca}) coefficients for sulfate (accumulation/dry-mode), titania and BC are plotted in Fig. 1 as a function of wavelength. For sulfate, the specific extinction coefficient (k_{ext}) at 500nm of 3200 m^2/kg and single scattering albedo (ω_o) of 1 reflects the non-absorbing properties of sulfate. Although titania's 500nm scattering efficiency (k_{sca} = 3850 m^2/kg) is greater than sulfate's in this instance, titania additionally absorbs SW radiation (k_{abs} = 2000 m^2/kg at 250 nm, and k_{abs} = 600 m^2/kg at 500 nm) which can be explained by the band-theory of solids [Yang et al., 2003]. Thus titania is partially absorbing. Our modelled BC efficiently absorbs SW radiation (k_{abs} = 8300 m^2/kg at 500nm) but also produces a non-negligible SW scattering effect (k_{sca} = 2500 m^2/kg at 500nm) which is comparable in magnitude to the equivalent scattering efficiency of both titania and sulfate. Therefore, to describe titania as an efficient light-scatterer and/or BC as an efficient light-absorber is an over-simplification.

Our choice of particle size and density will impact the aerosol's gravitational sedimentation rate and therefore its atmospheric residence time (the sedimentation rate is also a property of the local atmospheric conditions) [Rasch et al., 2008]. To determine the importance of our choice of aerosol properties, we have calculated the respective gravitational sedimentation rates by using the method of Pruppacher and Klett (1979) (which utilises Stoke's law) and incorporating temperature and pressure values from the International Standard Atmosphere [ICAO, 1993] (Fig. S1 in the Supplement). We find that the average sedimentation rates between 18-26 km altitude for our prescribed sulfate, titania, and BC are 23, 9.5 and 0.75 m/day respectively, and the equivalent rates between 26-30 km are 52, 22, and 1.8 m/day. Therefore, one would expect BC to be advected to much higher altitudes than sulfate in these simulations. For perspective, Schoeberl et al (2008) deduced from observations that the

atmospheric tropical vertical velocity between 18-26 km has an upper limit of 35 m/day, and the equivalent velocity between 26-30 km is below 61 m/day.

3 Method

We first validated the model's stratospheric sulfate scheme by simulating the Mt Pinatubo eruption and then comparing the results with observations. These simulations comprised a 10-member ensemble in which 20 Tg[SO_2] is injected between 16-18 km over a single day in June 1991, following the method of Aquila et al (2012). Figure 2a shows the global/annual-mean sulfate aerosol optical depth (AOD) anomaly for the HadGEM2-ensemble and for AVHRR and SAGE-II observations. The model clearly captures the peak AOD from the AVHRR data, and the exponential decline thereafter. Figures 2b-d show the zonal-mean AOD anomaly for the same time period. The agreement between the model and observed AOD is reasonable. Some differences in the temporal evolution of the AODs in the model and the observations are due to the almost concurrent eruption of Cerro Hudson which injected approximately 3.3Tg[SO_2] into the southern hemisphere [Deshler and Anderson-Sprecher, 2006]. This relatively close agreement between observations and HadGEM2 estimates, together with other modelling studies of other volcanic eruptions [Haywood et al., 2010] suggests that the model is a useful tool for stratospheric geoengineering simulations.

The geoengineering investigation was based on a 240-year Pre-Industrial Control simulation (forced by constant 1860's GHGs and aerosol emissions) and historical simulations for the period 1860-2005 following CMIP5 [Taylor et al., 2012] protocol followed by RCP8.5 emission specified from 2005-2019. Leading on from these simulations, we performed 3-member ensembles for the period 2020-2100 for: RCP8.5 only, RCP8.5 with SO_2 injection (geoSulf), RCP8.5 with TiO_2 injection (geoTiO_2), and RCP8.5 with BC injection (geoBC). Aerosol (or gaseous SO_2 for the geoSulf scenario) was injected at a constant rate between 23-28 km altitude in a single vertical column at the equator. The injection altitude and location were chosen to maximise the stratospheric lifetime of the aerosol, which is transported poleward by the upper branch of the Brewer-Dobson circulation [Niemeier et al., 2011], and therefore make the geoengineering approach reasonably efficient.

We inject aerosol at such a rate as to maintain the top-of-the-atmosphere (TOA) net radiation at piControl levels. Specifically, we define the TOA radiative flux Imbalance (TOA-Imb) as the annual/global-mean TOA net radiation (incoming SW minus outgoing

LW+SW) minus the average TOA net radiation of the piControl period. By sufficient aerosol injection, we aim to maintain TOA-Imb=0. This scenario represents our interpretation of 'equal amount of geoengineering' for each aerosol. The advantage of returning net radiation to piControl levels (rather than completely equilibrating TOA fluxes) is that piControl had already been simulated comprehensively for CMIP5 (240 model-years), hence permitting robust statistics to be calculated. The TOA radiative imbalance is a metric that satellites are able to measure (e.g. CERES [L'Ecuyer et al, 2015] and EarthCare [Illingworth et al, 2015]), albeit with +/- 3 W/m^2 accuracy at present [Priestley et al, 2011; von Schuckmann et al., 2016]. Therefore our target could be applicable to an actual SAI scenario. In contrast, Radiative Forcing (RF) (the net radiation perturbation at the tropopause from some external forcing, after stratospheric adjustment), cannot be directly measured by satellites and therefore it would be difficult to obtain a specified radiative forcing in an actual SAI scenario. Of course, other metrics could be chosen [e.g. MacMartin et al., 2013], with each metric having its own signal/noise characteristic.

To determine the injection rates required to maintain TOA-Imb balance, we first conducted 15-year atmosphere-only simulations of 1 Tg aerosol (or SO_2 for sulfate) injection per year to calculate the specific radiative effect for each aerosol. We then used the radiative effect to calculate the injection rate necessary to offset the RCP8.5 anthropogenic radiative forcing (ARF) for the 2020-2100 period (with ARF values from Meinshausen et al (2011)). We used the ARF to estimate the injection rates required to produce TOA-Imb=0 as this produces reasonable initial injection rates. As the geoengineering simulations progressed, we altered the injection rate when necessary to ensure that TOA-Imb balance was maintained (Fig. S2 in the Supplement). A detailed description of our methods is provided in the supplementary material (Section S2).

Our analysis focuses initially on the temporal evolution of the TOA-Imb and global mean temperature changes to show that our simulations provide plausible counterbalances to global mean temperature changes under RCP8.5. However, our main focus is on the differences between a recent historical period (1980-2005) (hereafter denoted HIST) and the geoengineering experiments during the period 2090-2100, with an emphasis on different geographical patterns. As we were not explicitly attempting to reach a specific global mean temperature, the choice of reference period was left until after the geoengineering

simulations had been completed. We then selected a recent historical period from which the 2090s global-mean temperature anomaly for geoSulf was negligible (Fig. 3b). The HIST period selected is close to the historical control period used in the IPCC AR5 report (1986-2005) [e.g. Fig. 12.10 from Collins et al., 2013] which facilitates comparison of our RCP8.5 climate changes with the CMIP5 multi-model means.

4 Results

4.1 Effectiveness at maintaining global mean TOA-Imb and near surface temperature

Figure 3 shows the global/annual-mean TOA-Imb and near-surface air temperature anomaly for the geoengineering and RCP8.5 simulations, with respect to the HIST period. For all of the geoengineering simulations we were able to maintain TOA-Imb≈0 for the entirety of the 80-year period (Fig. 3a). For geoSulf, geoTiO_2 and geoBC, the TOA-Imb was maintained within +/-0.21, +/-0.18 and +/-0.20 Wm^{-2}, respectively (1 standard deviation throughout the 2020-2100 period).

The near-surface global temperature response differs between the aerosols with a greater cooling trend for sulfate than for titania or BC (Fig. 3b). To determine the cause of the anomalous warming in geoBC, we assess the net radiation at the top of the atmosphere for 2020-2100. Fig. S3 in the Supplement shows the global-mean net-downward radiation anomaly for the geoengineering experiments, evaluated at the TOA and the tropopause; and the global-mean net-downward heat flux anomaly at the surface. The radiation changes at the TOA and tropopause, and the heat flux anomaly at the surface, are comparable for the geoSulf and geoTiO_2 experiments for the duration of 2020-2100. In contrast, geoBC exhibits an increasingly positive net radiation anomaly at the tropopause (+0.2 W/m^2 averaged over 2020-2100) despite the negligible TOA radiation anomaly. After stratospheric temperature adjustment, radiative perturbations at the TOA and tropopause are equal for a given climate forcing, which implies that the consistently non-adjusted stratosphere (due primarily to increasing aerosol injection rates) is responsible for the differences in TOA and tropopause radiative perturbations in geoBC. This implies that if we had injected aerosol sufficiently to produce an equal radiative effect at the tropopause, the temperature trends for the geoengineering experiments in Fig. 3 would have been more comparable. If we were to choose stabilisation of temperature as our basic metric, then one could approximate the results by simply scaling the results by the ratio of the

temperature perturbation relative to 1980-2005 to that for geoSulf. The scaling would be 1 (by design) for geoSulf, 1.1 for geoTiO_2 and 1.28 for geoBC. If the metric chosen were instead to keep the global mean precipitation the same, then the scaling would be 1 (by design) for geoSulf, 0.91 geoTiO_2 and 0.68 for geoBC. However, we shall see that the changes in many of the variables we consider are dominated by large scale changes in the spatial patterns of response rather than the 10-30% changes in magnitude of the response that applying such a scaling would induce. We therefore choose to present un-scaled results here but caveat that such a scaling could be applied should we wish to apply a different metric. From Fig. 3b, geoSulf exhibits a near-surface air cooling trend with respect to 2020 despite a net gain of atmospheric energy, which is likely due to an uneven vertical distribution of this energy gain.

Fig. 3c shows the global mean precipitation anomaly with respect to the HIST period. The precipitation reduction is greater for BC than for sulfate and titania, despite the positive temperature trend in geoBC (Fig. 3b). The hydrological sensitivity to geoengineering, defined as the global mean precipitation change per unit temperature change, is 2%/^{o}C for sulfate, 2.5%/^{o}C for titania, and 4.6%/^{o}C for BC. The hydrological sensitivity for RCP8.5 is 1.32 %/^{o}C, which is close to the CMIP5 ensemble-mean [Fig. 12.7 from Collins et al., 2013]. For comparison, Bala et al (2008) found a hydrological sensitivity of 2.4%/^{o}C for solar irradiance reduction and 1.4%/^{o}C for CO_2 increase.

4.2 Aerosol distribution

The time-averaged injection rates for the 2090s period are 14 Tg[SO_2]/yr, 5.8 Tg/yr and 0.81 Tg/yr for geoSulf, geoTiO_2 and geoBC, respectively. This SO_2 injection rate is approximately equivalent to 1 Mt Pinatubo eruption per year [Dhomse et al., 2014]. These injection rates equate to global aerosol mass-burden anomalies of 49.5, 20.2, and 5.1 Tg for geoSulf, geoTiO_2 and geoBC, respectively. The geoBC mass burden is comparable to the equilibrium burdens of the high-altitude (HA) and small-radius (SmR) experiments from Kravitz et al (2012), although they injected BC at a constant rate of 1 Tg/yr, around 20% higher than in our study. Figure 4 shows the 2090s annual, June-July-August (JJA) and December-January-February (DJF) aerosol mass concentration anomalies (annual mean aerosol optical depths are shown in Fig. S4 in the Supplement). Peak sulfate concentrations are found at the injection region at the equator (Figs. 4a,d,g) and over the winter pole. Titania and BC reach greater altitudes than sulfate (>50 km), which is due to their smaller size-distributions and self-lofting

from SW-absorption [Kravitz et al., 2012]. While sulfate aerosol concentrations are highest at the equator, the highest concentrations of BC are found in the polar stratosphere. This is because the larger particle size of the sulfate aerosol is subject to a larger sedimentation velocity (Fig. S1 in the Supplement) and thus a greater fraction of aerosol is removed close to the source region. The results from titania suggest a spatial distribution intermediate between sulfate and BC owing to the intermediate size distribution.

Figure 5 shows the total annual, JJA and DJF aerosol deposition anomalies averaged over the 2090s (the seasonal cycle of the deposition anomalies are shown in Fig. S5 in the Supplement). Sulfate is predominantly deposited in the Northern Hemisphere (NH) extratropics in the boreal spring and summer (Fig. 5d) which is likely attributable to tropopause fold events in the lower branch of the Brewer-Dobson circulation (BDC) [Kravitz et al., 2012]. In contrast, Titania and BC are primarily deposited at high latitudes in the polar winter, which is attributable to the diabatic descent of air in the deep branch of the BDC [e.g. Tegtmeier et al., 2008]. Kravitz et al (2012) also found in their SmR experiment that BC deposition was limited to the polar regions, but their maximum deposition was during polar summer rather than polar winter. The global/annual-mean deposition rates of sulfate and BC from geoengineering are 37 and 1.5 mg/m^2/yr, respectively. These amounts may be compared with 231 and 12.7 mg/m^2/yr from non-geoengineering sources, amounting to increases of 16 % and 12 % respectively. The global/annual-mean deposition rate for titania is 11 mg/m^2/yr.

4.3 Temperature and precipitation

Figure 6 shows the annual mean near-surface air temperature (Figs. 6a-d) and precipitation anomalies (Figs. 6e-h) with respect to HIST. RCP8.5 (Fig. 6a) shows the typical global warming signal of amplified warming at high-latitudes due to temperature feedbacks [Pithan and Mauritsen, 2014] and the surface-albedo feedback [e.g. Kharin et al., 2013]. This results in an annual mean warming of +11.3 ^{o}C averaged over the Arctic region (> 60 ^{o}N) and an average NH land warming of +7.3 ^{o}C. This figure provides an alarming picture of the change in global mean temperature by the end of this century should global society follow the RCP8.5 (essentially a business as usual) pathway. All 3 SAI experiments produce a surface-cooling with respect to RCP8.5, with geoSulf exhibiting the greatest global-mean cooling effect of -4.85 ^{o}C, considering TOA-Imb is balanced for each geoengineering experiment. The latitudinal distribution of cooling varies markedly between the SAI

experiments, with relative tropical cooling for geoSulf and geoTiO_2 (Figs. 6b,d) and polar cooling for geoBC (Fig. 6c). Defining the 'SAI cooling effect' as the temperature difference between SAI and RCP8.5, the ratio of cooling effect at high latitudes (> 60^o) between geoBC and geoSulf is 1.19 and between geoBC and geoTiO_2 is 1.23. In the tropics and mid-latitudes (< 60^o) the equivalent ratios are 0.64 and 0.71 respectively. The high-latitude cooling in the case of geoBC is attributable to the zonal distribution of BC (Figs. 4c,f,i) which is more evenly spread over the stratosphere than for geoSulf and geoTiO_2. The result is a greater surface SW forcing at high-latitudes in the summer hemisphere for geoBC. For instance, in the Arctic (>60^oN) in JJA, the surface SW forcing is -25.65 Wm^{-2} in geoBC and -3.3 and -6.55 Wm^{-2} in geoSulf and geoTiO_2 respectively. Although the global-mean precipitation rate increases for the RCP8.5 scenario (Fig. 6e), certain regions such as the Amazon basin exhibit a drying trend. This is in line with the CMIP5 multi-model projections documented in the Intergovernmental Panel on Climate Change 5^{th} assessment report (IPCC AR5) [e.g. Fig. 12.10 from Collins et al., 2013]. All of the SAI experiments show a global-mean precipitation reduction with respect to both HIST and RCP8.5 (Figs. 6f-h), which is due to the deceleration of the hydrological cycle and is a robust model response to SAI [e.g. Yu et al., 2015; Tilmes et al., 2013; Bala et al., 2008]. The magnitude of the precipitation changes are greater for geoBC than for geoSulf or geoTiO_2; for instance, the global mean precipitation anomaly is -0.26 mm/day for geoBC compared to -0.12 mm/day for geoSulf and -0.14 mm/day for geoTiO_2. In order to maintain TOA-Imb=0, BC must produce a greater SW perturbation at the tropopause and at the TOA than sulfate or titania, which is compensated by the increased LW perturbation resulting from stratospheric warming. The troposphere is relatively transparent to SW radiation but absorbs efficiently in the LW spectrum, therefore the annual-mean surface radiative forcing in the geoBC experiment is greater (-18.6 W m^{-2}) than for geoSulf or geoTiO_2 (-7.4 and -9.6 W m^{-2} respectively – see Fig. S6 in the Supplement). Bala et al (2008) showed that the magnitude of the precipitation response is dependent on the surface radiative imbalance; therefore the precipitation reduction is amplified in geoBC. It is important to note that if the RCP8.5 warming relative to HIST was completely offset in the geoBC and geoTiO_2 experiments, the hydrological response would be greater than in Fig. 6. Using the hydrological sensitivities calculated in section 4.1, the precipitation changes relative to HIST would be -0.34 mm/day for geoBC and -0.16 mm/day for geoTiO_2. From Fig. S6 in the Supplement, the reduction in surface SW flux in the RCP8.5 scenario is due to increases in water vapor [Haywood et al., 2011]. Haywood

et al (2011) report a clear-sky reduction of -5.7 W/m^2 while our study is consistent at a value of -5.4 W/m^2 (not plotted). However, in all geoengineering cases, this reduction is comprehensively overwhelmed by aerosol direct effects.

Figure 7 shows the JJA temperature (Figs. 7a-d) and precipitation (Figs. 7e-h) anomalies. In the geoSulf and geoTiO_2 scenarios, the temperature is effectively maintained at HIST levels (Figs. 7b,d). However, a slight bias towards high-latitude NH warming in geoSulf and geoTiO_2 results in a northward displacement of the Inter-Tropical Convergence Zone (ITCZ), which is exemplified by the Sahelian precipitation increase in Figs. 7f,h. This phenomenon was noted by Haywood et al (2013) and has been observed after large hemispherically asymmetric volcanic eruptions [Oman et al., 2006]. Although the general pattern of precipitation change is similar for the 3 SAI scenarios, geoBC again displays a greater drying signal, with 80% of the total land area experiencing a JJA precipitation reduction in geoBC compared to 70% for geoTiO_2, 57% for geoSulf and 52% for RCP8.5.

Figure 8 shows the DJF temperature (Figs. 8a-d) and precipitation (Figs. 8e-h) anomalies. The temperature reduction over Greenland in geoBC (Fig. 8c) is due to the significant decrease in downwelling SW radiation at the surface during the Arctic sea-ice formation season (September-October-November), which leads to a positive sea-ice albedo feedback and further localised cooling. This inference is corroborated by Fig. 9, which shows the Arctic DJF sea-ice extent in terms of the average DJF sea-ice boundary (the Antarctic DJF sea-ice extent is shown in Fig. S7 in the Supplement). The sea-ice boundary in geoBC (Fig. 9c) extends to well below Greenland, and the total sea-ice extent anomaly is +1.72 million km^2 which vastly exceeds the HIST standard deviation of +/- 0.52 million km^2. In comparison, the sea-ice extent anomaly of -11 million km^2 for RCP8.5 (Fig. 9a) marks a reduction by 43% of the total HIST sea-ice extent. Returning to Fig. 8, the poleward shift in the NH extratropical rain-belt over the Atlantic in RCP8.5 (Fig. 8e) is a robust result of GHG-induced global warming and is related to storm track displacement [Lombardo et al., 2015]. This same response is evident in the geoengineering simulations (Figs. 8f-h), although to a much lesser extent in geoSulf and geoTiO_2.

4.4 Stratospheric changes

Figure 10 shows the zonal-mean temperature change as a function of latitude and altitude for the JJA and DJF seasons. The stratospheric cooling in conjunction with tropospheric warming

in RCP8.5 (Figs. 10a,e) is a robust result of increasing GHG-concentrations [e.g. Schmidt et al., 2013]. Aerosols directly affect temperature by absorbing radiation, and indirectly by scattering radiation and by ambient dynamical and chemical changes [Carslaw and Kärcher, 2006]. Sulfate predominantly absorbs in the LW and near-infra-red spectrum (Fig. 1a). The stratospheric radiative heating in geoSulf is most pronounced in the tropical region, where sulfate absorbs outgoing LW radiation from the warm troposphere below, and then emits comparatively less radiation from the ambient cold stratosphere [Ferraro et al., 2011]. In contrast, titania and BC absorb in both the SW and LW spectrum (Figs. 1b,c), and therefore preferentially warm the summer-hemisphere and tropical stratosphere, where solar radiation is most prevalent. geoBC produces the most significant warming effect, with an average stratospheric (15-50 km altitude) temperature increase of +33 ^{o}C and a maximum temperature increase of +68 ^{o}C, which occurs in JJA (Figs. 10c,g). The maximum BC-induced heating relative to the baseline RCP8.5 scenario is +76 ^{o}C (Fig. S8 in the Supplement), which is comparable to the ~80 ^{o}C temperature change Kravitz et al (2012) found in their SmR scenario. For comparison, the maximum sulfate-induced and titania-induced heating relative to RCP8.5 are far more modest at +7 ^{o}C and +22 ^{o}C, respectively.

A warming of the lower tropical stratosphere could have multiple climatic repercussions such as a weakening of the tropospheric tropical circulation [Ferraro et al., 2014], strengthening of the polar vortex [Driscoll et al., 2012] and modification of the Quasi-Biennial Oscillation (QBO) [Aquila et al., 2014]. Additionally, an increase in the Tropical Tropopause Layer (TTL) temperature would increase the specific humidity of air entering the stratosphere [Dessler et al., 2013]. Changes to the stratospheric water vapor content could have significant chemical and radiative impacts, contributing to ozone depletion via the HO_x cycle and stratospheric warming via LW-absorption [Kravitz et al., 2012]. To assess the effects of geoengineering on stratospheric water vapor, we calculate the time-averaged H_2O mixing ratio averaged between 20^{o}S-20^{o}N and 16-20 km altitude. In the HIST era, the H_2O MMR is 4.2 ppmv, in close agreement with HALOE observations [Gettelman et al., 2010]. In the 2090s, the average H_2O MMR is 6.3 ppmv for RCP8.5, 4.8 ppmv for geoSulf, 7.1 ppmv for geoTiO_2, and 32.7 ppmv for geoBC. The stratospheric water vapor feedback is therefore greater for geoBC and geoTiO2 than for geoSulf.

A strengthening of the polar vortex could be instigated by an increased temperature gradient between the tropical/mid-latitude and polar stratospheres, a phenomenon which was observed

after the Pinatubo eruption [Stenchikov et al., 2002]. We concentrate on the Arctic wintertime (DJF) response to SAI, and adopt a similar metric to that used by Ferraro et al (2011) to determine the stratospheric temperature gradient. Explicitly, we determine the difference in temperature between 20^{o}N-20^{o}S (Tropics) and 50^{o}N-90^{o}N (North Pole) at 17-22 km altitude in the DJF season. Using this metric, the change in temperature gradients for geoBC, geoSulf and geoTiO_2 are +10.4 ^{o}C, +7 ^{o}C, and +10.1 ^{o}C, respectively, indicating a steeper temperature gradient between the tropics and poles. Additionally, Fig. 11 shows the 50hPa DJF geopotential height anomalies over the Arctic for RCP8.5 and the 3 SAI experiments. The negative geopotential height anomaly centered over the North Pole in all the SAI experiments is indicative of a strengthened polar night jet and a positive Arctic Oscillation phase [Stenchikov et al., 2002]. The DJF zonal-mean zonal-wind anomaly (Fig. S9 in the Supplement) substantiates our inference of a strengthened polar-night jet under SAI, with increased zonal windspeeds at 65^{o}N / 40km altitude of 62 m/s, 17 m/s, and 37 m/s for geoBC, geoSulf, and geoTiO_2 respectively.

The Quasi-Biennial Oscillation (QBO) is a periodic change in the equatorial zonal wind pattern in the stratosphere, which fluctuates between easterly and westerly-shear phases [Baldwin et al., 2001]. Aquila et al (2014) showed that radiative heating in the aerosol layer could prolong the westerly-phase of the QBO (where the phase is defined at 40 hPa) by enhancing the residual-mean upwelling motion and strengthening the westerly winds. HadGEM2-CCS includes a non-orographic gravity wave scheme that permits the model to internally generate a QBO and is therefore capable of assessing QBO changes [The HadGEM2 Development Team, 2011]. The average QBO period for the HIST-era ensemble is 27 months (Fig. S10 in the Supplement) which agrees closely with observations [e.g. Baldwin et al., 2001]. Figure 12 shows the 2090s QBO timeseries for one ensemble member of the RCP8.5 and SAI experiments (Figs. S11a,b in the Supplement show the QBO timeseries for the other 2 ensemble members). The average QBO periods for this timespan, which are determined using all 3-ensemble members, are 20 months for RCP8.5, 31 months for geoSulf and 36 months for geoTiO_2. For geoBC, no QBO-like oscillation can be detected in the 10-year time span, suggesting a persistent westerly-phase such as observed by Aquila et al (2014) in their $G_5^{22\text{-}25km}$ scenario. In their HadGEM2-CC simulations, Kawatani and Hamilton (2013) also observed a decline in the QBO period for the RCP8.5 scenario, although they were unable to provide a reason for this. A robust inference from this

work is that the magnitude of SAI's impact on stratospheric zonal winds correlates with the magnitude of the stratospheric warming.

5 Discussion

In this work, we have assessed the climatic impacts of sulfate, black carbon and titania-injection against a baseline RCP8.5 scenario, by comparing the 2090s climate with a simulated historical period. We have shown that, although the distribution of climate changes are similar for the 3 SAI scenarios, the magnitude of the changes differ, for instance BC produces a substantially greater stratospheric warming signal with concomitantly greater changes to stratospheric dynamics. The severity of the stratospheric temperature changes effectively excludes BC from being a viable option for geoengineering. Additionally, we have shown that producing an equivalent top of the atmosphere radiative perturbation with a SW-absorbing aerosol such as BC (or to a lesser extent titania) compared to a SW-scattering aerosol such as sulfate, induces a comparatively greater SW forcing at the surface. Bala et al (2008) showed that reduced latent heat fluxes compensate for the SW reduction at the surface, instigating a deceleration of the hydrological cycle that is proportional to the magnitude of the SW reduction. This explains the comparatively greater precipitation reduction exhibited by geoBC in figures 6-8. Our results complement Niemeier et al (2013), who showed that a LW-absorbing sulfate layer would produce a greater hydrological perturbation per TOA SW forcing than a simple solar irradiance reduction scenario. The geoBC scenario displays a greater cooling at high-latitudes than the geoSulf and geoTiO_2 scenarios (Figs. 6-8), which comparatively exhibit a net tropical cooling. This raises the question of whether a combination of aerosols could potentially be injected to produce a zonally-homogeneous cooling if necessary. Although SAI with sulfate and titania effectively maintains the regional distribution of temperature at HIST levels, with a slight residual warming at high latitudes, the hydrological cycle decelerates substantially in all SAI scenarios which is exemplified by a global-mean reduction in precipitation. However, annual-minimum sea-ice extent in both hemispheres and global-mean thermosteric sea-level (Fig. S12 in the Supplement) are almost entirely maintained at HIST levels for all SAI scenarios.

We find that sulfate induces less stratospheric warming than titania. In contrast, Ferraro et al (2011) found that the peak stratospheric warming for titania was approximately a third of that from sulfate. Although the different climatologies, model configurations, and aerosol spatial

distributions will contribute to the difference in stratospheric temperature adjustment between our and Ferraro's work, the primary reason for the disparity is likely to be the aerosol size distributions. Our titania is smaller (median radius = 0.045 μm compared to 0.1 μm for Ferraro et al (2011)) and therefore scatters and absorbs SW more efficiently, producing a greater localised 'solar' warming. Their sulfate distribution contains a larger spread (σ = 2.0 for Ferraro et al (2011) compared to σ = 1.25 here), resulting in more coarse-mode particles and greater LW absorption. This disparity highlights the sensitivity of climatic effects to the specified aerosol size distribution. On a separate note, Ferraro et al (2011) neglected to alter the aerosol density component in the calculation of their aerosol masses and specific optical properties [A. Ferraro, personal communication]. The density that they used for all the aerosols of 1000 kg/m^3 is arguably applicable to black carbon, but not to sulfate and titania (which instead are ~1600 and ~4000 kg/m^3). Therefore, their aerosol burdens for sulfate and titania should be multiplied by 1.6 and 4 respectively, and their optical coefficients divided by 1.6 and 4, to obtain appropriate values.

It is important to note that the climate impacts described in section 4 are dependent on the optical properties of the aerosol, which are further dependent on the aerosol particle's size, shape, and composition [e.g. Kravitz et al., 2012]. In this investigation, the dry-mode size distribution of the aerosol species is held constant and hygroscopic growth is not represented in the BC and titania schemes, nor are the effects of internal mixing represented. Observations have shown that fresh BC aerosol is predominantly hydrophobic, but the uptake of soluble particulates (e.g. secondary organics) results in increased hygroscopicity [Liu et al., 2013]. Mineral dust, which contains 1-10% titania by mass [Ndour et al., 2008], exhibits low hygroscopicity for radii < 0.1 μm and similar growth to equivalently-sized sulfate aerosol thereafter [Koehler et al., 2009]. Although the historical stratospheric water vapor content is low (~4.2 ppmv in the tropical lower stratosphere during the HIST period), aerosol-induced stratospheric warming in the TTL would increase the specific humidity of air entering the stratosphere, therefore impacting hygroscopic growth. The injection of aerosol into pre-existing aerosol layers would lead to larger particles through coagulation and condensation, which would further alter the aerosol's optical and physical properties. The actual size of the aerosol in an SAI scheme would therefore depend on the injection strategy (e.g. location/ season) and the size and composition of the injected species [e.g. Carslaw and Kärcher, 2006; Heckendorn et al., 2009]. Recent research from Heckendorn et al (2009), Pierce et al (2010), English et al (2012), and

Weisenstein et al (2015) have highlighted the importance of representing aerosol growth in SAI simulations. A detailed assessment of the aerosol microphysics for sulfate, BC, and titania injection is not within the scope of this paper, but presents an important subject for future work.

The climatic impacts described in section 4 are specific to geoengineering against a baseline RCP8.5 scenario. If instead we had used a middle-of-the-road GHG-concentrations scenario such as RCP4.5 [Taylor et al., 2012], as used in the first tier of GeoMIP scenarios [Kravitz et al., 2011], then less aerosol-injection would be needed to obtain TOA-Imb=0 and therefore the aerosol deposition rates and atmospheric mass concentrations would be less than those reported in section 4. One would expect that the magnitude of stratospheric temperature changes (Fig. 8) and therefore zonal-mean zonal wind changes (Fig. 12) would be much less for each of the aerosols, possibly confounding the conclusions giving here relating to their comparative efficacy. An estimate for the amount of SAI required for RCP4.5 can be garnered from integrating the temperature anomalies for RCP8.5 and RCP4.5 for the period 2020-2100. The ratio of the integrated temperature anomalies for RCP4.5 to RCP8.5 is 0.43, hence we can assume that the injection rates required for RCP4.5 are ~0.43 of those for RCP8.5, producing a climate perturbation ~0.43 times as great. A further set of simulations, which instead utilise RCP4.5 as the baseline scenario, would be required to test this hypothesis.

We have used prescribed ozone fields in these simulations because representing stratospheric chemistry is prohibitively computationally expensive for the multiple centennial simulations performed here [The HadGEM2 development team, 2011]. Kravitz et al (2012) showed that BC injection could potentially result in global ozone depletion of >50%, therefore the chemistry changes in SAI could potentially exceed the importance of the physical changes in terms of climatic impacts (e.g. UV radiation at the surface). Tilmes et al (2012) showed that SW-scattering by geoengineered sulfate could potentially compensate for ozone-loss by back-scattering UV radiation in the tropics, but that this effect was insufficiently compensatory at high latitudes. Their result was scenario-dependent; ozone loss due to heterogeneous chemistry is enhanced for smaller particles and in the presence of higher free-radical concentrations. Therefore, additional research is needed in order to understand the effects on atmospheric chemistry of injecting alternative aerosols. This work has already been started for titania by Tang et al (2014).

Another important aspect of SAI which is comparatively under-researched is the potential for impacts on human health. Aerosol concentrations in the air near the surface are of interest because of potential human respiratory impacts [Robock, 2008]. For instance, the USA's National Institute for Occupational Safety and Health (NIOSH) recommends maximum exposure limits of 0.3 mg m^{-3} for ultrafine titania particles (radius <0.05 μm) and 2.4 mg m^{-3} for fine particles (radius < 1.5 μm) [Dankovic et al., 2011]. After undergoing coagulation and ageing in the atmosphere, it is likely that the second exposure limit is more applicable to this work. In our simulations, the maximum 2090's near-surface air concentration of titania (e.g. Fig. 4) for land regions between 60^oS-60^oN is 254 ng/m^3, which is of the order of 10^2 less than the NIOSH 'fine-particle' exposure limit. The equivalent maximum concentration anomalies of BC in geoBC and SO_4 in geoSulf are 10 ng/m^3 and 1851 ng/m^3 respectively. More work is needed to assess the potential impacts of SAI on air quality and human health.

Another thus far unmentioned aspect of this research is the potential for surface albedo modification by aerosol deposition. In particular, BC deposition on snow reduces the snow albedo through enhanced snow-melt and the coarsening of snow grains, which results in amplified high-latitude warming [Marks and King, 2013]. HadGEM2-CCS does not include the BC-on-snow feedback; therefore we estimate it by comparing the deposition rates for 2090s geoBC with the historical period. Jiao et al (2014) report that the simulated annual mean Arctic (>60^oN) BC deposition for the 2006-2009 period ranges from 13-35x10^7 kg/yr for the AEROCOM Phase II models. The annual mean Arctic BC deposition for the 2006-2009 period from our HadGEM2-CCS simulations is 23x10^7 kg/yr, which is within the AEROCOM range. The annual mean Arctic BC deposition anomaly for the 2090s period in geoBC is 19.6x10^7 kg/yr. Therefore, the effects of dirty snow in such an SAI scenario would likely be significant, which would have impacts on the distribution of temperature, particularly at high latitudes, potentially confounding some of our conclusions.

This research has highlighted potential climate impacts of injecting various stratospheric aerosols in order to ameliorate global warming. However, further research is needed to further assess the climatic impacts of stratospheric aerosol injection such as the impacts on ozone. Whilst research indicates that SAI is capable of averting certain climate changes such as surface-warming, SAI provides no amelioration for other climate impacts, such as ocean acidification. It is therefore important to note that the safest possible solution to avoiding the

sort of climate change instantiated by (e.g.) Fig. 6a of this report is to effectively mitigate greenhouse-gas emissions.

Author contribution

ACJ designed the experiments, performed the simulations, analysed the data, and wrote the manuscript with guidance and advice from JMH and AJ.

Data sets

Data used to generate figures, graphs, plots and tables are freely available via contacting the lead author: aj247@exeter.ac.uk.

Acknowledgements

The authors would like to thank Valentina Aquila for supplying AVHRR and SAGE data, and to Peter Cox, Angus Ferraro, David Keith and Alan Robock for helpful discussions. We also thank 2 anonymous reviewers and John Dykema for their comments and suggestions. ACJ was supported by a Met Office/NERC CASE (ref. 580009183) PhD studentship; JMH and AJ were supported by the Joint UK DECC/Defra Met Office Hadley Centre Climate Programme (GA01101).

References

d'Almeida, G. A., Koepke, P., and, Shettle, E. P.: Atmospheric aerosols: global climatology and radiative characteristics, A. Deepak Publishing, Hampton, USA, 1991.

Aquila, V., Oman, L. D., Stolarski, R. S., Colarco, P. R., and Newman, P. A.: Dispersion of the volcanic sulfate cloud from a Mount Pinatubo–like eruption, J. Geophys. Res., 117, D06216, doi:10.1029/2011JD016968., 2012.

Aquila, V., Garfinkel, C. I., Newman, P. A., Oman, L. D., and Waugh, D. W.: Modifications of the quasi-biennial oscillation by a geoengineering perturbation of the stratospheric aerosol layer, Geophys. Res. Lett., 41, 1738–1744, doi:10.1002/2013GL058818., 2014.

Bala, G., Duffy, P. B., and Taylor, K. E.: Impact of geoengineering schemes on the global hydrological cycle, P. Natl. Acad. Sci. USA., June 3 2008, vol. 105, no. 22, 7664-7669, 2008.

Baldwin, M. P., Gray, L. J., Dunkerton, T. J., Hamilton, K., Haynes, P. H., Randel, W. J., Holton, J. R., Alexander, M. J., Hirota, I., Horinouchi, T., Jones, D. B. A., Kinnersley, J. S., Marquardt, C., Sato, K., and Takahashi, M.: The quasi-biennial oscillation, Rev. Geophys., 39(2), 179–229, doi:10.1029/1999RG000073., 2001.

Bellouin, N., Boucher, O., Haywood, J., Johnson, C., Jones, A., Rae, J., and Woodward, S.: Improved representation of aerosols for HadGEM2, Hadley Centre technical note 73, Hadley Centre, Met Office, Exeter, UK, 42pp., available at http://www.metoffice.gov.uk/media/pdf/8/f/HCTN_73.pdf (last accessed 01/16), 2007.

Bellouin, N., Rae, J., Johnson, C., Haywood, J., Jones, A., and Boucher, O.: Aerosol forcing in the Hadley Centre CMIP5 simulations by HadGEM2-ES and the role of ammonium nitrate, J. Geophys. Res., 116, D20206, doi:10.1029/2011JD016074, 2011.

Berdahl, M., Robock, A., Ji, D., Moore, J. C., Jones, A., Kravitz, B., and Watanabe, S.: Arctic cryosphere response in the Geoengineering Model Intercomparison Project G3 and G4 scenarios, J. Geophys. Res. Atmos., 119, 1308–1321, doi:10.1002/2013JD020627., 2014.

Carslaw, K. C., and Kärcher, B.: Stratospheric aerosol processes, in Assessment of Stratospheric Aerosol Properties, edited by L. Thomason and T. Peter, WCRP 124, WMO/TD 1295, SPARC Rep. 4, World. Meteorol. Organ., Geneva, Switzerland, 2006.

Collins, M., Knutti, R., Arblaster, J., Dufresne, J.-L., Fichefet, T., Friedlingstein, P., Gao, X., Gutowski, W. J., Johns, T., Krinner, G., Shongwe, M., Tebaldi, C., Weaver, A. J., and

Wehner, M.: Long-term Climate Change: Projections, Commitments and Irreversibility. In: Climate Change 2013: The Physical Science Basis. Contribution of Working Group I to the Fifth Assessment Report of the Intergovernmental Panel on Climate Change [Stocker, T.F., Qin, D., Plattner, G.-K., Tignor, M., Allen, S. K., Boschung, J., Nauels, A., Xia, Y., Bex, V., and Midgley, P.M. (eds.)]. Cambridge University Press, Cambridge, United Kingdom and New York, NY, USA., 2013.

Crutzen, P.: Albedo Enhancement by Stratospheric Sulfur Injections: A Contribution to Resolve a Policy Dilemma?, Climatic Change, August 2006, Volume 77, Issue 3, pp 211-220, 2006.

Dankovic, D., Kuempel, E., Geraci, C., Gilbert, S., Rice, F., Schulte, P., Smith, R., Sofge, C., Wheeler, M., Lentz, T. J., Zumwalde, R., Maynard, A., Attfield, M., Pinheiro, G., Ruder, A., Hubbs, A., Ahlers, H., Lynch, D., Toraason, M., and Vallyathan, V.: Current intelligence bulletin 63: occupational exposure to titanium dioxide., Cincinnati, OH: U.S. Department of Health and Human Services, Public Health Service, Centers for Disease Control and Prevention, National Institute for Occupational Safety and Health, DHHS (NIOSH) Publication No. 2011-160, 2011 Apr; :1-119, 2011.

Davies, T., Cullen, M. J. P., Malcolm, A. J., Mawson, M. H., Staniforth, A., White, A. A., and Wood, N.: A new dynamical core for the Met Office's global and regional modelling of the atmosphere, Q. J. R. Meteorol. Soc., 131, pp. 1759–1782, doi: 10.1256/qj.04.101, 2005

Deepak, A., and Gerber, H. E. (Eds.): Report of the experts meeting on aerosols and their climatic effects (Williamsburg, Virginia, March 1983), Rep. WCP-55, World Clim. Programme, World Meteorol. Organ., Geneva, 1983.

Dessler, A. E., Schoeberl, M. R., Wang, T., Davis, S. M., and Rosenlof, K. H.: Stratospheric water vapor feedback, Proc. Natl. Acad. Sci. U.S.A., 110, 45, 18087-18091, doi: 10.1073/pnas.1310344110, 2013.

Dhomse, S. S., Emmerson, K. M., Mann, G. W., Bellouin, N., Carslaw, K. S., Chipperfield, M. P., Hommel, R., Abraham, N. L., Telford, P., Braesicke, P., Dalvi, M., Johnson, C. E., O'Connor, F., Morgenstern, O., Pyle, J. A., Deshler, T., Zawodny, J. M., and Thomason, L. W.: Aerosol microphysics simulations of the Mt.~Pinatubo eruption with the UM-UKCA composition-climate model, Atmos. Chem. Phys., 14, 11221-11246, doi:10.5194/acp-14-11221-2014, 2014.

Deshler, T., and Anderson-Sprecher, R.: Non-volcanic stratospheric aerosol trends: 1971–2004, in Assessment of Stratospheric Aerosol Properties, edited by L. Thomason and T. Peter, WCRP 124, WMO/TD 1295, SPARC Rep. 4, World Meteorolo. Organ., Geneva, Switzerland, 2006.

Driscoll, S., Bozzo, A., Gray, L. J., Robock, A., and Stenchikov, G.: Coupled Model Intercomparison Project 5 (CMIP5) simulations of climate following volcanic eruptions, J. Geophys. Res. Atmos., 117, D17105, doi:10.1029/2012JD017607, 2012.

L'Ecuyer, T. S., Beaudoing, H. K., Rodell, M., Olson, W., Lin, B., Kato, S., Clayson, C. A., Wood, E., Sheffield, J., Adler, R., Huffman, G., Bosilovich, M., Gu, G., Robertson, F., Houser, P. R., Chambers, D., Famiglietti, J. S., Fetzer, E., Liu, W. T., Gao, X., Schlosser, C. A., Clark, E., Lettenmaier, D. P., and Hilburn, K.: The Observed State of the Energy Budget in the Early Twenty-First Century. J. Climate, 28, 8319–8346., doi:http://dx.doi.org/10.1175/JCLI-D-14-00556.1, 2015.

English, J. M., Toon, O. B., and Mills, M. J.: Microphysical simulations of sulfur burdens from stratospheric sulfur geoengineering, Atmos. Chem. Phys., 12, 4775–4793, doi:10.5194/acp-12-4775-2012, 2012.

Ferraro, A. J., Highwood, E. J., and Charlton-Perez, A. J.: Stratospheric heating by potential geoengineering aerosols, Geophys. Res. Lett., 38, L24706, doi:10.1029/2011GL049761., 2011.

Ferraro, A. J., Highwood, E. J., and Charlton-Perez, A. J.: Weakened tropical circulation and reduced precipitation in response to geoengineering, Environ. Res. Lett., 9, 014001, 2014.

Forster, P., Ramaswamy, V., Artaxo, P., Berntsen, T., Betts, R., Fahey, D. W., Haywood, J., Lean, J., Lowe, D. C., Myhre, G., Nganga, J., Prinn, R., Raga, G., Schulz, M., and Van Dorland, R.: Changes in Atmospheric Constituents and in Radiative Forcing. In: Climate Change 2007: The Physical Science Basis. Contribution of Working Group I to the Fourth Assessment Report of the Intergovernmental Panel on Climate Change [Solomon, S., Qin, D., Manning, M., Chen, Z., Marquis, M., Averyt, K. B., Tignor, M., and Miller, H. L. (eds.)]. Cambridge University Press, Cambridge, United Kingdom and New York, NY, USA., 2007.

Gettelman, A., Hegglin, M. I., Son, S.-W., Kim, J., Fujiwara, M., Birner, T.,Kremser, S., Rex, M., Añel, J. A., Akiyoshi, H., Austin, J., Bekki, S., Braesike, P.,Brühl, C., Butchart, N., Chipperfield, M., Dameris, M., Dhomse, S., Garny, H.,Hardiman, S. C., Jöckel, P., Kinnison, D. E., Lamarque, J. F., Mancini, E., Marchand, M., Michou, M., Morgenstern, O., Pawson, S., Pitari, G., Plummer, D.,Pyle, J. A., Rozanov, E., Scinocca, J., Shepherd, T. G., Shibata, K., Smale, D., Teyssèdre, H., and Tian, W.: Multimodel assessment of the upper troposphere and lower stratosphere: Tropics and global trends, J. Geophys. Res., 115, D00M08, doi:10.1029/2009JD013638, 2010.

The HadGEM2 Development Team: Martin, G. M., Bellouin, N., Collins, W. J., Culverwell, I. D., Halloran, P.R., Hardiman, S. C., Hinton, T. J., Jones, C. D., McDonald, R. E., McLaren, A. J., O'Connor, F. M., Roberts, M. J., Rodriguez, J. M., Woodward, S., Best, M. J., Brooks, M. E., Brown, A. R., Butchart, N., Dearden, C., Derbyshire, S. H., Dharssi, I., Doutriaux-Boucher, M., Edwards, J. M., Falloon, P. D., Gedney, N., Gray, L. J., Hewitt, H. T., Hobson, M., Huddleston, M. R., Hughes, J., Ineson, S., Ingram, W. J., James, P. M., Johns, T. C., Johnson, C. E., Jones, A., Jones, C. P., Joshi, M. M., Keen, A. B., Liddicoat, S., Lock, A. P., Maidens, A. V., Manners, J. C., Milton, S. F., Rae, J. G. L., Ridley, J. K., Sellar, A., Senior, C. A., Totterdell, I. J., Verhoef, A., Vidale, P. L., and Wiltshire, A.: The HadGEM2 family of Met Office Unified Model climate configurations, Geosci. Model Dev., 4, 723–757, www.geosci-model-dev.net/4/723/2011/, doi:10.5194/gmd-4-723-2011, 2011.

Haywood, J.M., Jones, A., Clarisse, L., Bourassa, A., Barnes, J., Telford, P., Bellouin N., Boucher, O., Agnew, P., Clerbaux, C., Coheur, P., Degenstein, D., and Braesicke, P.: Observations of the eruption of the Sarychev volcano and simulations using the HadGEM2 climate model, J. Geophys. Res., 115, D21212, doi:10.1029/2010JD014447, 2010.

Haywood, J. M., Bellouin, N., Jones, A., Boucher, O., Wild, M., and Shine, K. P.: The roles of aerosol, water vapor and cloud in future global dimming/brightening, J. Geophys. Res., 116, D20203, doi:10.1029/2011JD016000., 2011.

Haywood, J.M., Jones, A., Bellouin, N., and Stephenson, D.: Asymmetric forcing from stratospheric aerosols impacts Sahelian rainfall, Nat. Clim. Change, 3, 660–665, doi:10.1038/nclimate1857, 2013.

Heckendorn, P., Weisenstein, D., Fueglistaler, S., Luo, B. P., Rozanov, E., Schraner, M., Thomason, L. W., and Peter, T.: The impact of geoengineering aerosols on stratospheric

temperature and ozone, Environ. Res. Lett., 4, 045108, doi:10.1088/1748-9326/4/4/045108, 2009.

Illingworth, A. J., Barker, H. W., Beljaars, A., Ceccaldi, M., Chepfer, H., Clerbaux, N., Cole, J., Delanoë, J., Domenech, C., Donovan, D. P., Fukuda, S., Hirakata, M., Hogan, R. J., Huenerbein, A., Kollias, P., Kubota, T., Nakajima, T., Nakajima, T. Y., Nishizawa, T., Ohno, Y., Okamoto, H., Oki, R., Sato, K., Satoh, M., Shephard, M. W., Velázquez-Blázquez, A., Wandinger, U., Wehr, T., and van Zadelhoff, G.-J.: The EarthCARE Satellite: The Next Step Forward in Global Measurements of Clouds, Aerosols, Precipitation, and Radiation, Bull. Amer. Meteor. Soc., 96, 1311–1332. doi: http://dx.doi.org/10.1175/BAMS-D-12-00227.1, 2015.

International Civil Aviation Organisation (ICAO): Manual of the ICAO Standard Atmosphere: extended to 80 kilometres (262 200 feet), Doc 7488/3, Third ed., 1993

Jiao, C., Flanner, M. G., Balkanski, Y., Bauer, S. E., Bellouin, N., Berntsen, T. K., Bian, H., Carslaw, K. S., Chin, M., De Luca, N., Diehl, T., Ghan, S. J., Iversen, T., Kirkevåg, A., Koch, D., Liu, X., Mann, G. W., Penner, J. E., Pitari, G., Schulz, M., Seland, Ø., Skeie, R. B., Steenrod, S. D., Stier, P., Takemura, T., Tsigaridis, K., van Noije, T., Yun, Y., and Zhang, K.: An AeroCom assessment of black carbon in Arctic snow and sea ice, Atmos. Chem. Phys., 14, 2399–2417, doi:10.5194/acp-14-2399-2014, 2014.

Kawatani, Y., and Hamilton, K.: Weakened stratospheric quasibiennial oscillation driven by increased tropical mean upwelling, Nature, 497, 478–481, doi:10.1038/nature12140, 2013.

Kharin, V. V., Zwiers, F. W., Zhang, X., and Wehner, M.: Changes in temperature and precipitation extremes in the CMIP5 ensemble, Climatic Change (2013) 119:345–357, DOI 10.1007/s10584-013-0705-8, 2013.

Koehler, K. A., Kreidenweis, S. M., DeMott, P. J., Petters, M. D., Prenni, A. J., and Carrico, C. M.: Hygroscopicity and cloud droplet activation of mineral dust aerosol, Geophys. Res. Lett., 36, L08805, doi:10.1029/2009GL037348., 2009.

Kravitz, B., Robock, A., Boucher, O., Schmidt, H., Taylor, K. E., Stenchikov, G., and Schulz, M.: The Geoengineering Model Intercomparison Project (GeoMIP). Atmosph. Sci. Lett., 12: 162–167. doi: 10.1002/asl.316, 2011.

Kravitz, B., Robock, A., Shindell, D. T., and Miller, M. A.: Sensitivity of stratospheric geoengineering with black carbon to aerosol size and altitude of injection, J. Geophys. Res., 117, D09203, doi:10.1029/2011JD017341., 2012.

Kravitz, B., Robock, A., Forster, P. M., Haywood, J. M., Lawrence, M. G., and Schmidt, H.: An overview of the Geoengineering Model Intercomparison Project (GeoMIP), J. Geophys. Res. Atmos., 118, 13,103–13,107, doi:10.1002/2013JD020569, 2013.

Kravitz, B., Robock, A., Tilmes, S., Boucher, O., English, J. M., Irvine, P. J., Jones, A., Lawrence, M. G., MacCracken, M., Muri, H., Moore, J. C., Niemeier, U., Phipps, S. J., Sillmann, J., Storelvmo, T., Wang, H., and Watanabe, S.: The Geoengineering Model Intercomparison Project Phase 6 (GeoMIP6): simulation design and preliminary results, Geosci. Model Dev., 8, 3379-3392, doi:10.5194/gmd-8-3379-2015, 2015.

Liu, D., Allan, J., Whitehead, J., Young, D., Flynn, M., Coe, H., McFiggans, G., Fleming, Z. L., and Bandy, B.: Ambient black carbon particle hygroscopic properties controlled by mixing state and composition, Atmos. Chem. Phys., 13, 2015-2029, doi:10.5194/acp-13-2015-2013, 2013.

Lombardo, K., Colle, B. A., and Zhang, Z.: Evaluation of Historical and Future Cool Season Precipitation over the Eastern United States and Western Atlantic Storm Track Using CMIP5 Models. J. Climate, 28, 451–467., doi: http://dx.doi.org/10.1175/JCLI-D-14-00343.1, 2015.

MacMartin, D.G., Keith, D.W., Kravitz, B., and Caldeira, K.: Management of trade-offs in geoengineering through optimal choice of non-uniform radiative forcing, Nat. Clim. Change, 3, 365-368, doi:10.1038/nclimate1722, 2013.

Marks, A. A., and King, M. D.: The effect of snow/sea ice type on the response of albedo and light penetration depth (e-folding depth) to increasing black carbon, The Cryosphere, 8, 1625–1638, www.the-cryosphere.net/8/1625/2014/, doi:10.5194/tc-8-1625-2014, 2014.

Meinshausen, M., Smith, S. J., Calvin, K. V., Daniel, J. S., Kainuma, M. L. T., Lamarque, J.-F., Matsumoto, K., Montzka, S. A., Raper, S. C. B., Riahi, K., Thomson, A. M., Velders, G. J. M., and Vuuren, D. Van:. "The RCP Greenhouse Gas Concentrations and their Extension from 1765 to 2300." Climatic Change (Special Issue), DOI: 10.1007/s10584-011-0156-z, 2011.

Ndour, M., D'Anna, B., George, C., Ka, O., Balkanski, Y., Kleffmann, J., Stemmler, K., and Ammann, M.: Photoenhanced uptake of NO_2 on mineral dust: Laboratory experiments and model simulations, Geophys. Res. Lett., 35, L05812, doi:10.1029/2007GL032006., 2008.

Niemeier, U., Schmidt, H., and Timmreck, C.: The dependency of geoengineered sulfate aerosol on the emission strategy, Atmos. Sci. Lett., 12, 189–194, doi:10.1002/asl.304, 2011.

Niemeier, U., Schmidt, H., Alterskjær, K., and Kristjánsson, J. E.: Solar irradiance reduction via climate engineering: Impact of different techniques on the energy balance and the hydrological cycle, J. Geophys. Res. Atmos., 118, 11,905–11, 917, doi:10.1002/2013JD020445., 2013.

Oman, L., Robock, A., Stenchikov, G. L. & Thordarson, T.: High-latitude eruptions cast shadow over the African monsoon and the flow of the Nile., Geophys. Res. Lett., 33, L18711 16, 2006.

Peters, G. P., Andrew, R. M., Boden, T., Canadell, J. G., Ciais, P., Le Quéré, C., Marland, G., Raupach, M. R., and Wilson, C.: The challenge to keep global warming below 2 °C, Nat. Clim. Change, 3, 4-6, doi:10.1038/nclimate1783, 2013

Pierce, J. R., D. K. Weisenstein, P. Heckendorn, T. Peter, and D. W. Keith (2010), Efficient formation of stratospheric aerosol for climate engineering by emission of condensible vapor from aircraft, Geophys. Res. Lett., 37, L18805, doi:10.1029/2010GL043975.

Pitari, G., Aquila, V., Kravitz, B., Robock, A., Watanabe, S., Cionni, I., De Luca, N., Di Genova, G., Mancini, E., and Tilmes, S.: Stratospheric ozone response to sulfate geoengineering: Results from the Geoengineering Model Intercomparison Project (GeoMIP), J. Geophys. Res. Atmos., 119, 2629–2653, doi:10.1002/2013JD020566., 2014.

Pithan, F., and Mauritsen, T.: Arctic amplification dominated by temperature feedbacks in contemporary climate models, Nat. Geosci., 7, 181-184, doi:10.1038/ngeo2071, 2014.

Pope, F. D., Braesicke, P., Grainger, R. G., Kalberer, M., Watson, I. M., Davidson, P. J., and Cox, R. A.: Stratospheric aerosol particles and solar-radiation management, Nature Climate Change, 2, 713–719, doi:10.1038/nclimate1528, 2012.

Priestley, K. J., Smith, G. L., Thomas, S., Cooper, D., Lee III, R. B., Walikainen, D., Hess, P., Szewczyk, Z. P., and Wilson, R.: Radiometric Performance of the CERES Earth Radiation

Budget Climate Record Sensors on the EOS Aqua and Terra Spacecraft through April 2007, J. Atmos. Oceanic Technol., 28, 3–21, doi: http://dx.doi.org/10.1175/2010JTECHA1521.1, 2011.

Pruppacher, H.R., and Klett, J.D.: Microphysics of Clouds and Precipitation, D. Reidel Publishing Company, Dordretch, ISBN: 978-90-277-1106-9, Holland, Reprinted 1980.

Rasch, P. J., Tilmes, S., Turco, R. P., Robock, A., Oman, L., Chen, C.-C., Stenchikov, G. L., and Garcia, R. R.: An overview of geoengineering of climate using stratospheric sulphate aerosols, Phil. Trans. R. Soc. A 2008 366 4007-4037; DOI: 10.1098/rsta.2008.0131, 2008.

Ribarsky, M. W.: Titanium dioxide, in Handbook of Optical Constants of Solids, edited by E. Palik, pp. 795–804, Academic, Orlando, Fla, 1985.

Robock, A., Oman, L., and Stenchikov, G. L.: Regional climate responses to geoengineering with tropical and Arctic SO2 injections. J. Geophys. Res. 113, D16101 doi:10.1029/2008JD010050., 2008.

Schmidt, H., Rast, S., Bunzel, F., Esch, M., Giorgetta, M., Kinne, S., Krismer, T., Stenchikov, G., Timmreck, S., Tomassini, L., and Walz, M.: Response of the middle atmosphere to anthropogenic and natural forcings in the CMIP5 simulations with the Max Planck Institute Earth system model, J. Adv. Model. EarthSyst., 5, 98–116, doi:10.1002/jame.2001, 2013.

Schoeberl, M. R., Douglass, A. R., Stolarski, R. S., Pawson, S., Strahan, S. E., and Read, W.: Comparison of lower stratospheric tropical mean vertical velocities, J. Geophys. Res., 113, D24109, doi:10.1029/2008JD010221., 2008.

von Schuckmann, K., Palmer, M.D., Trenberth, K.E., Cazenave, A., Chambers, D., Champollion, N., Hansen, J., Josey, S.A., Loeb, N., Mathieu, P.-P., Meyssignac, B., and Wild, M.: An imperative to monitor Earth's energy imbalance, Nat. Clim. Change, 6, 138–144, doi:10.1038/nclimate2876, 2016.

Shepherd, J., et al.: Geoengineering the climate: Science, governance, and uncertainty. Royal Society Policy document 10/09, 82 pp, ISBN: 978-0-85403-773-5, 2009.

Stenchikov, G., Robock, A., Ramaswamy, V., Schwarzkopf, M. D., Hamilton, K., and Ramachandran, S.: Arctic Oscillation response to the 1991 Mount Pinatubo eruption: Effects of volcanic aerosols and ozone depletion, J. Geophys. Res., 107(D24), 4803, doi:10.1029/2002JD002090, 2002.

Tang, M. J., Telford, P. J., Pope, F. D., Rkiouak, L., Abraham, N. L., Archibald, A. T., Braesicke, P., Pyle, J. A., McGregor, J., Watson, I. M., Cox, R. A., and Kalberer, M.: Heterogeneous reaction of N2O5 with airborne TiO2 particles and its implication for stratospheric particle injection, Atmos. Chem. Phys., 14, 6035-6048, doi:10.5194/acp-14-6035-2014, 2014.

Taylor, K. E., Stouffer, R. J., and Meehl, G. A.: An Overview of CMIP5 and the Experiment Design, Bull. Amer. Meteor. Soc., 93, 485–498, doi: http://dx.doi.org/10.1175/BAMS-D-11-00094.1, 2012.

Tegtmeier, S., Kruger, K., Wohltmann, I., Schoellhammer, K., and Rex, M.: Variations of the residual circulation in the Northern Hemispheric winter, J. Geophys. Res., 113, D16109, doi:10.1029/2007JD009518., 2008.

Teller, E., Wood, L., and Hyde, R.: Global Warming and Ice Ages: I. Prospects for Physics-Based Modulation of Global Change, Lawrence Livermore National Laboratory Publication UCRL-JC-128715, 18 pp., 1997.

Tilmes, S., Garcia, R. R., Kinnison, D. E., Gettelman, A., and Rasch, P. J.: Impact of geoengineered aerosols on the troposphere and stratosphere, J. Geophys. Res., 114, D12305, doi:10.1029/2008JD011420, 2009.

Tilmes, S., Kinnison, D. E., Garcia, R. R., Salawitch, R., Canty, T., Lee-Taylor, J., Madronich, S., and Chance, K.: Impact of very short-lived halogens on stratospheric ozone abundance and UV radiation in a geo-engineered atmosphere, Atmos. Chem. Phys., 12, 10945-10955, doi:10.5194/acp-12-10945-2012, 2012.

Tilmes, S., Fasullo, J., Lamarque, J.-F., Marsh, D. R., Mills, M., Alterskjær, K., Muri, H., Kristjánsson, J. E., Boucher, O., Schulz, M., Cole, J. N. S., Curry, C. L., Jones, A., Haywood, J., Irvine, P. J., Ji, D., Moore, J. C., Karam, D. B., Kravitz, B., Rasch, P. J., Singh, C., Yoon, J.-H., Niemeier, U., Schmidt, H., Robock, A., Yang, S., and Watanabe, S.: The hydrological impact of geoengineering in the Geoengineering Model Intercomparison Project (GeoMIP), J. Geophys. Res. Atmos., 118, 11,036–11,058, doi:10.1002/jgrd.50868., 2013.

Weisenstein, D. K., Keith, D. W., and Dykema, J. A.: Solar geoengineering using solid aerosol in the stratosphere, Atmos. Chem. Phys., 15, 11835-11859, doi:10.5194/acp-15-11835-2015, 2015.

Yang, H., Zhu, S., and Pan, N.: Studying the Mechanisms of Titanium Dioxide as Ultraviolet-Blocking Additive for Films and Fabrics by an Improved Scheme, Journal of Applied Polymer Science, Vol. 92, 3201–3210, 2004.

Yu, X., Moore, J. C., Cui, X., Rinke, A., Ji, D., Kravitz, B., and Yoon, J.-H.: Impacts, effectiveness and regional inequalities of the GeoMIP G1 to G4 solar radiation management scenarios, Global and Planetary Change, 129, 10–22, http://dx.doi.org/10.1016/j.gloplacha.2015.02.010, 2015.

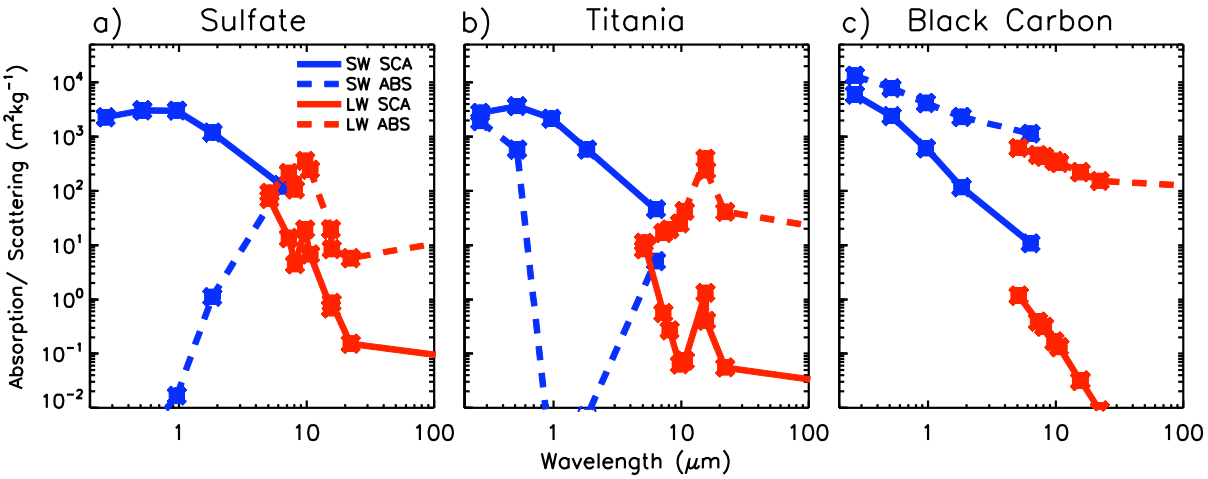

Figure 1. *Optical properties as a function of wavelength for a) accumulation-mode sulfate, b) titania, c) black carbon. Points are plotted at the middle of each spectral waveband, as detailed in Bellouin et al (2007)*

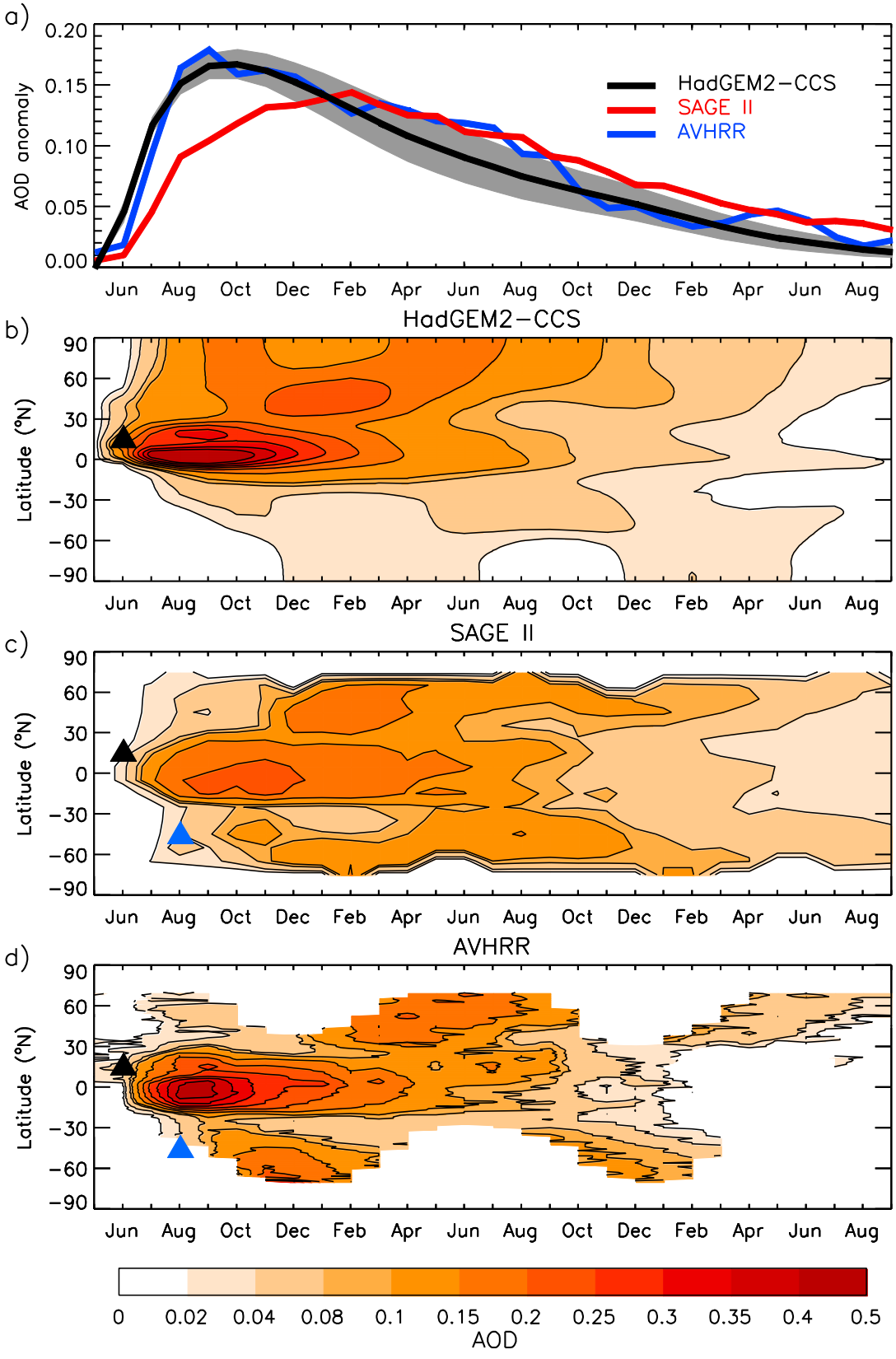

Figure 2. *a) 75°S-75°N-mean 550nm sulfate AOD anomaly for the Pinatubo simulations and observations, b-d) timeseries of zonal-mean 550nm sulfate AOD anomaly*

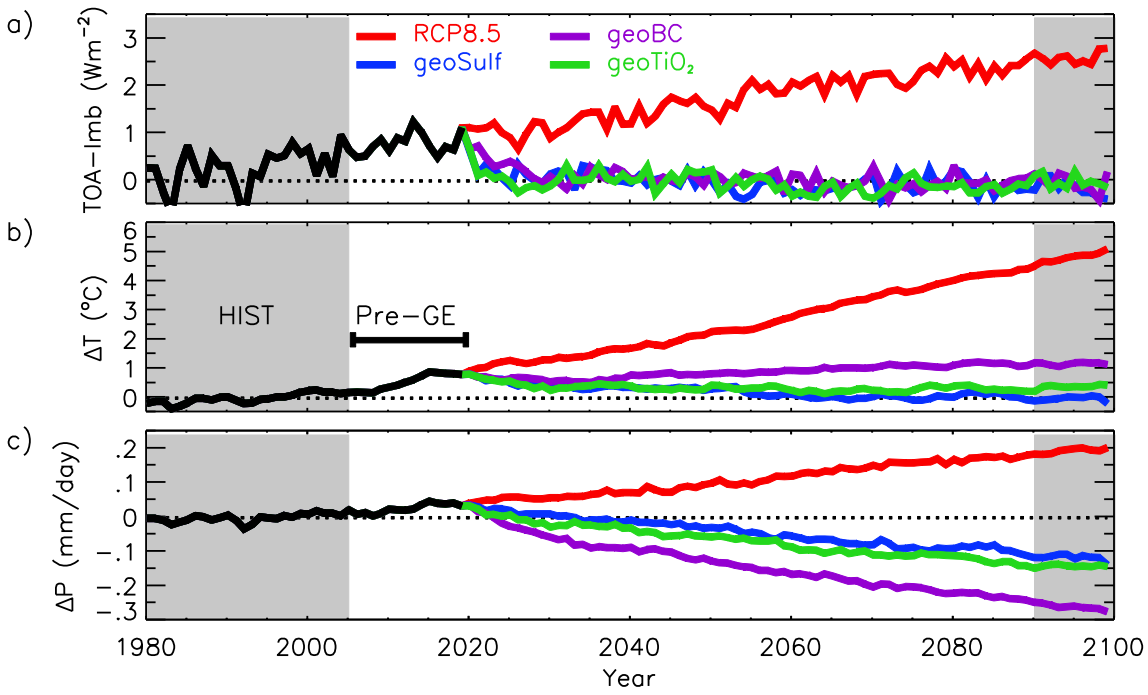

Figure 3. *Timeseries of annual/global-mean a) top-of-the-atmosphere radiative flux anomaly with respect to the pre-industrial control simulation b) near-surface air temperature anomaly with respect to the HIST period c) global mean precipitation anomaly with respect to HIST*

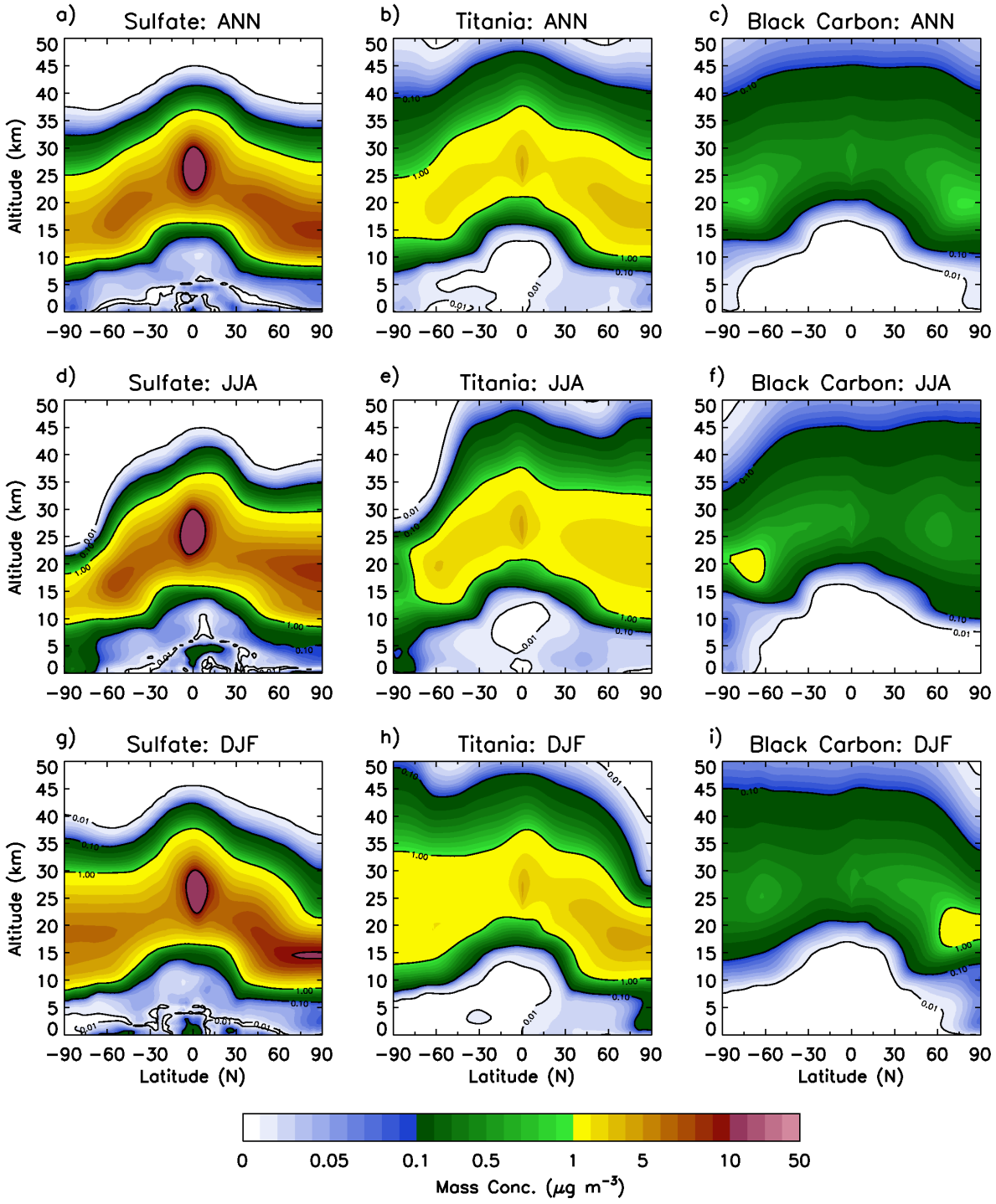

Figure 4. *Annual and seasonal zonal-mean mass concentration anomalies for sulfate (geoSulf - left), titania (geoTiO_2 - centre) and black carbon (geoBC - right)*

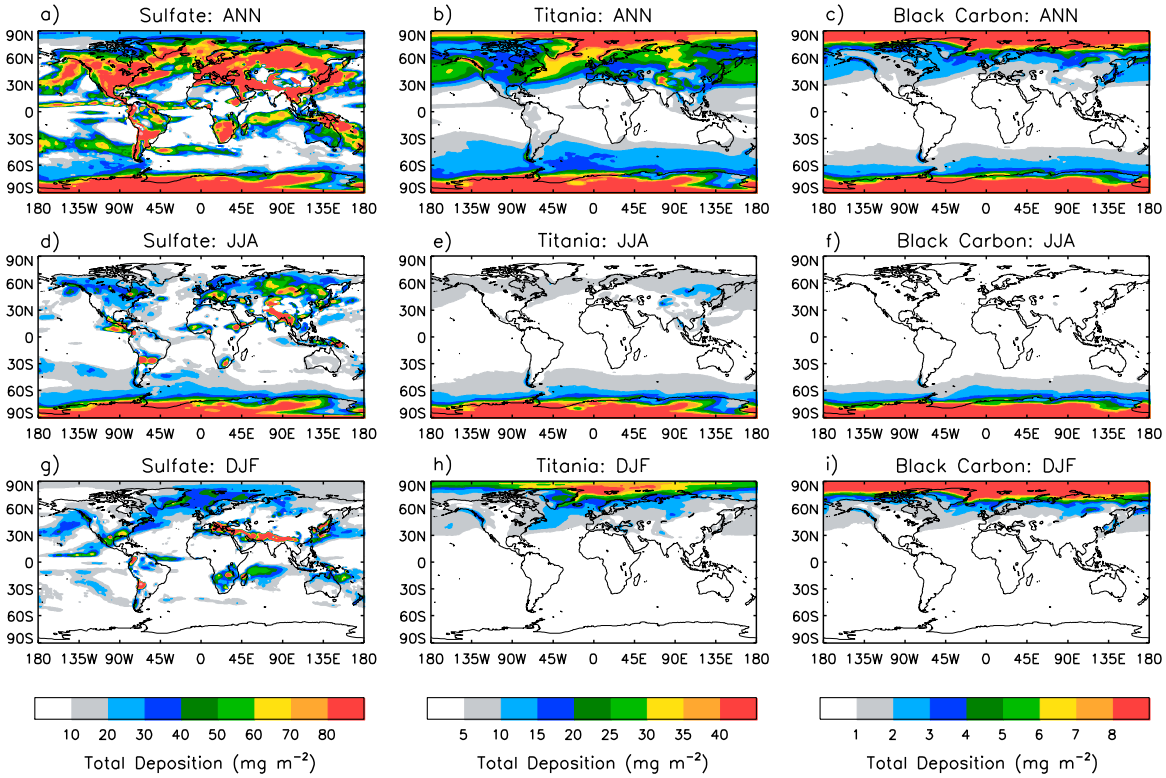

Figure 5. *Annual and seasonal total deposition anomalies (in units of mg m^{-2} yr^{-1} and 0.25x mg m^{-2} yr^{-1} respectively)*

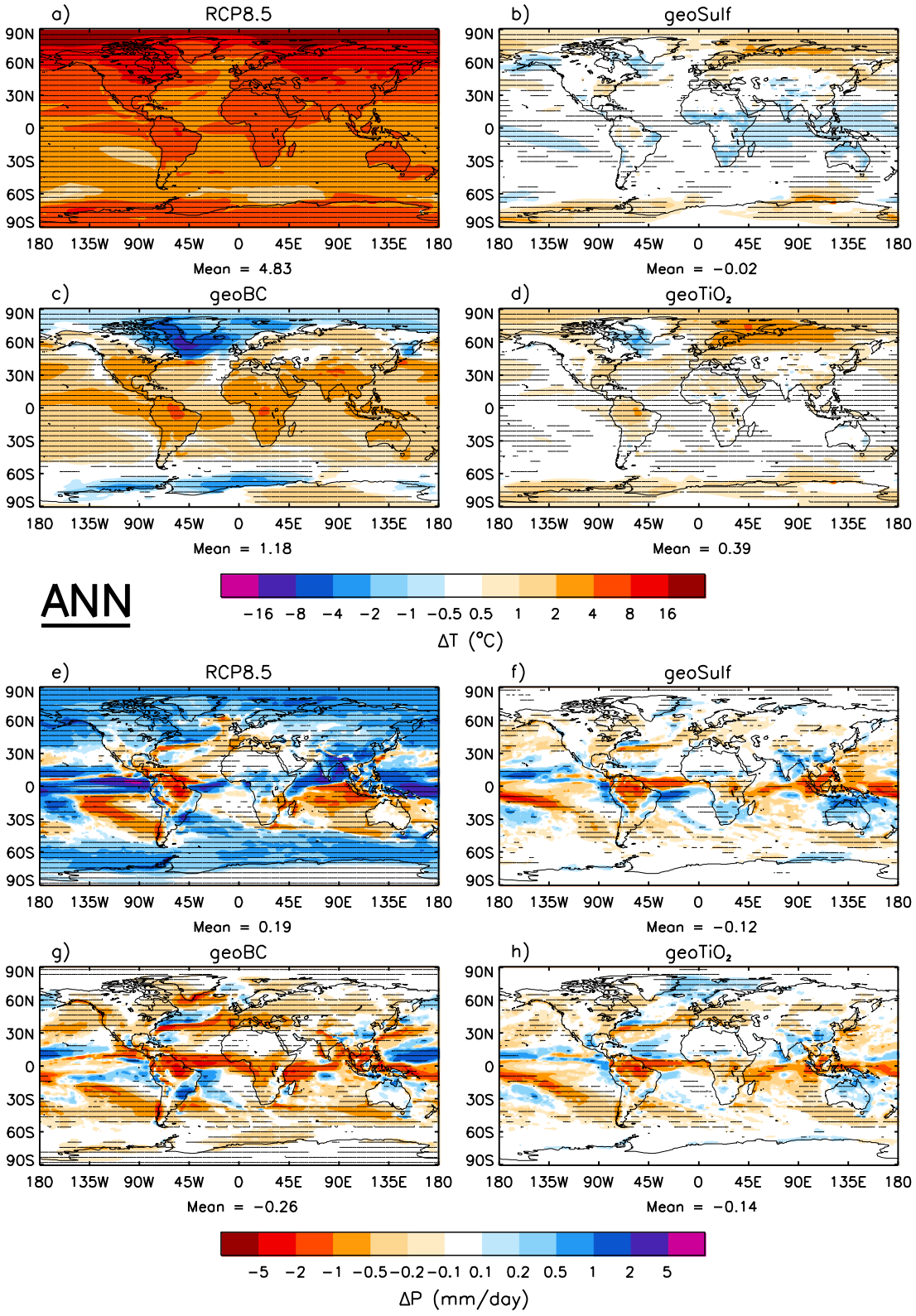

Figure 6. *Annual-mean near-surface air temperature (top) and precipitation rate (bottom) anomalies with respect to HIST. Stipling indicates where changes are significant at the 5% level using a two-tailed Student's t-test*

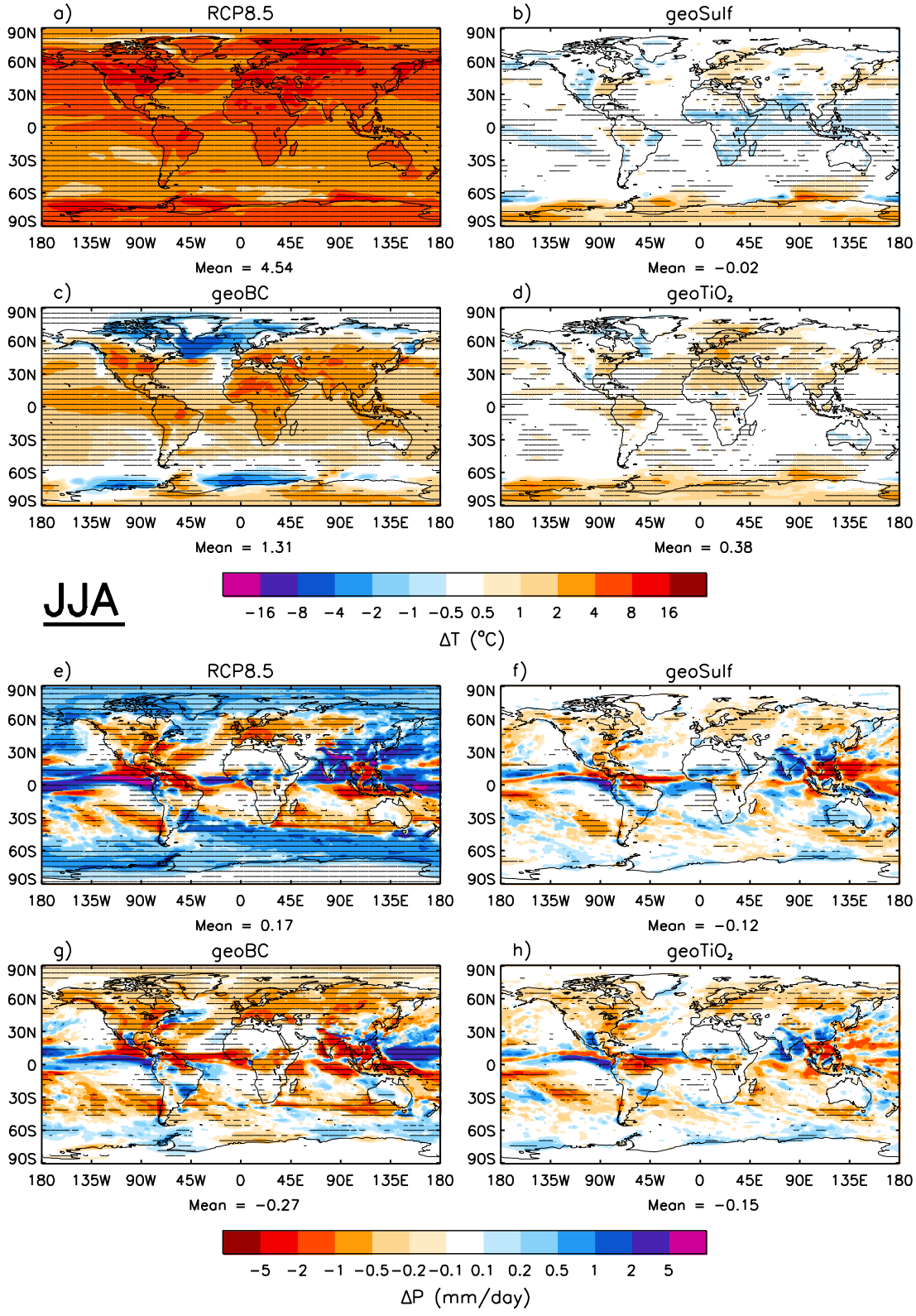

Figure 7. *JJA near-surface air temperature (top) and precipitation rate (bottom) anomalies with respect to HIST*

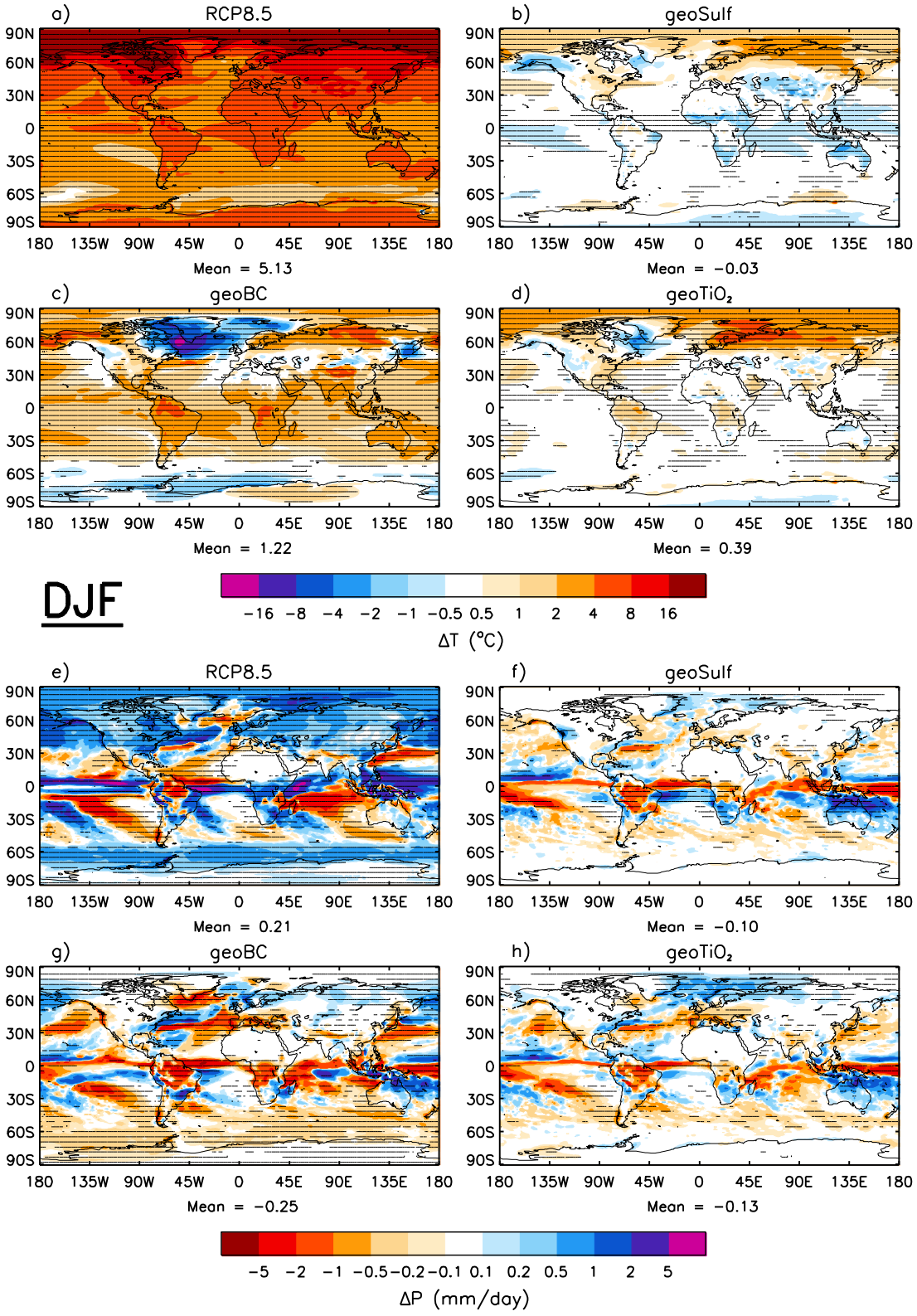

Figure 8. *DJF near-surface air temperature (top) and precipitation rate (bottom) anomalies with respect to HIST*

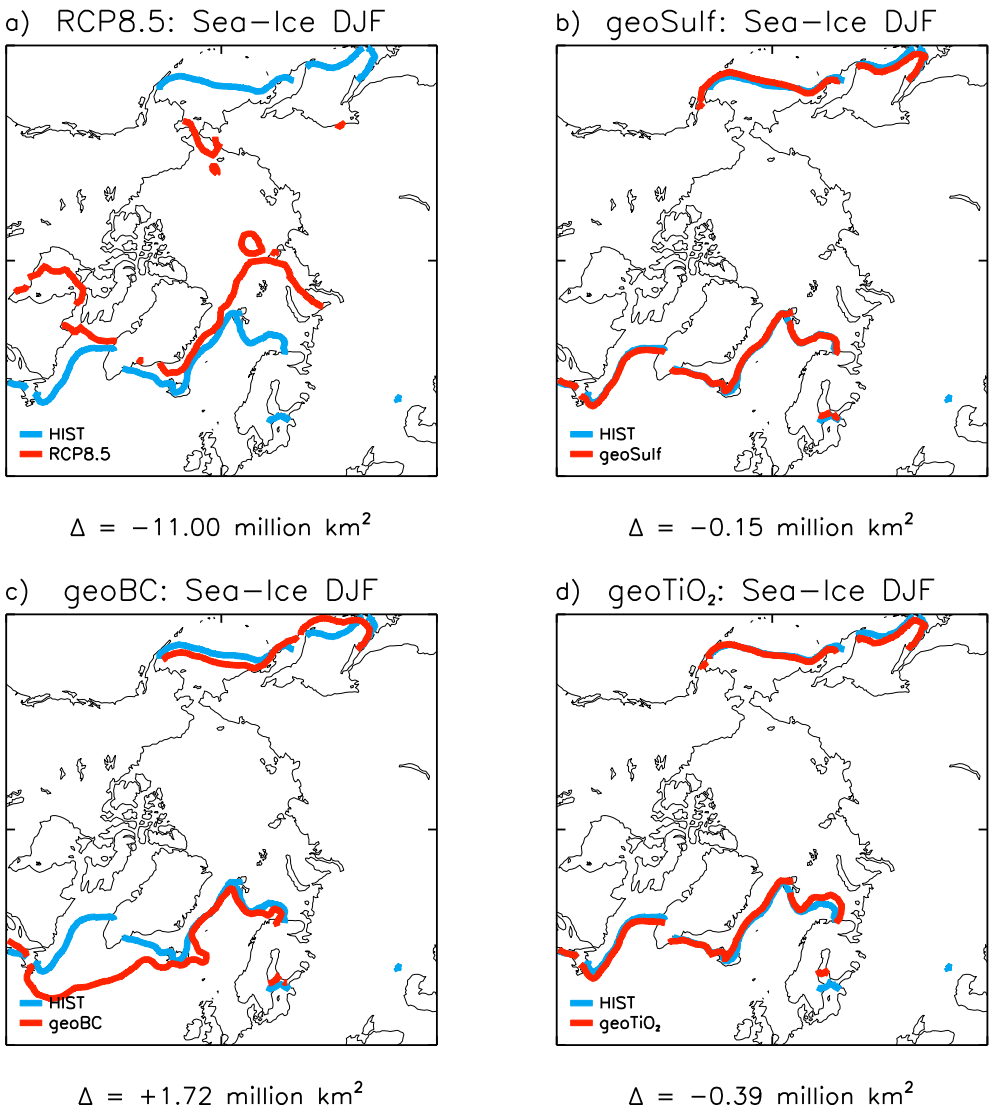

1

2 **Figure 9.** *DJF northern-hemisphere sea-ice edge plotted with the HIST extent*

3

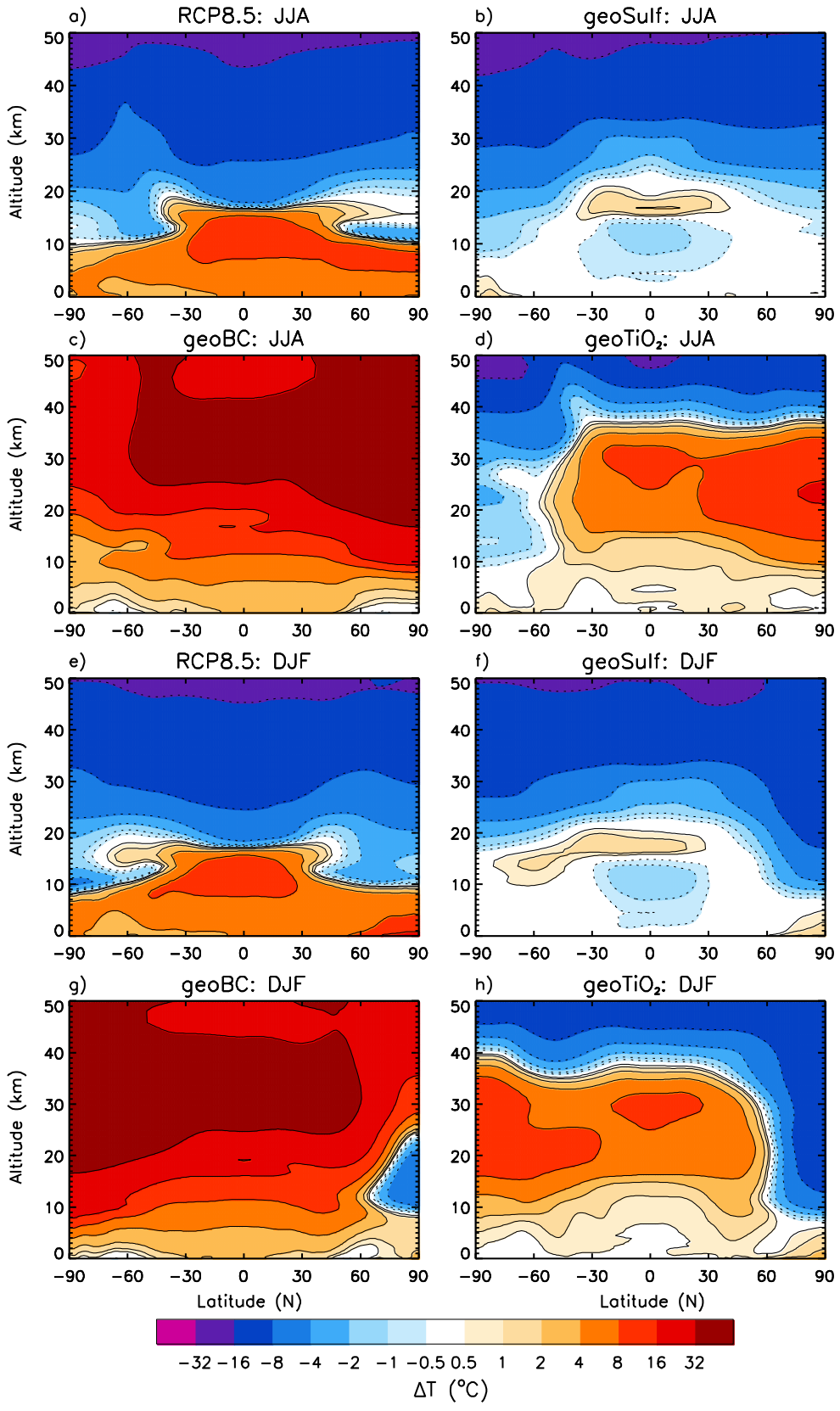

Figure 10. *JJA (top) and DJF (bottom) zonal-mean temperature anomaly with altitude, with respect to HIST*

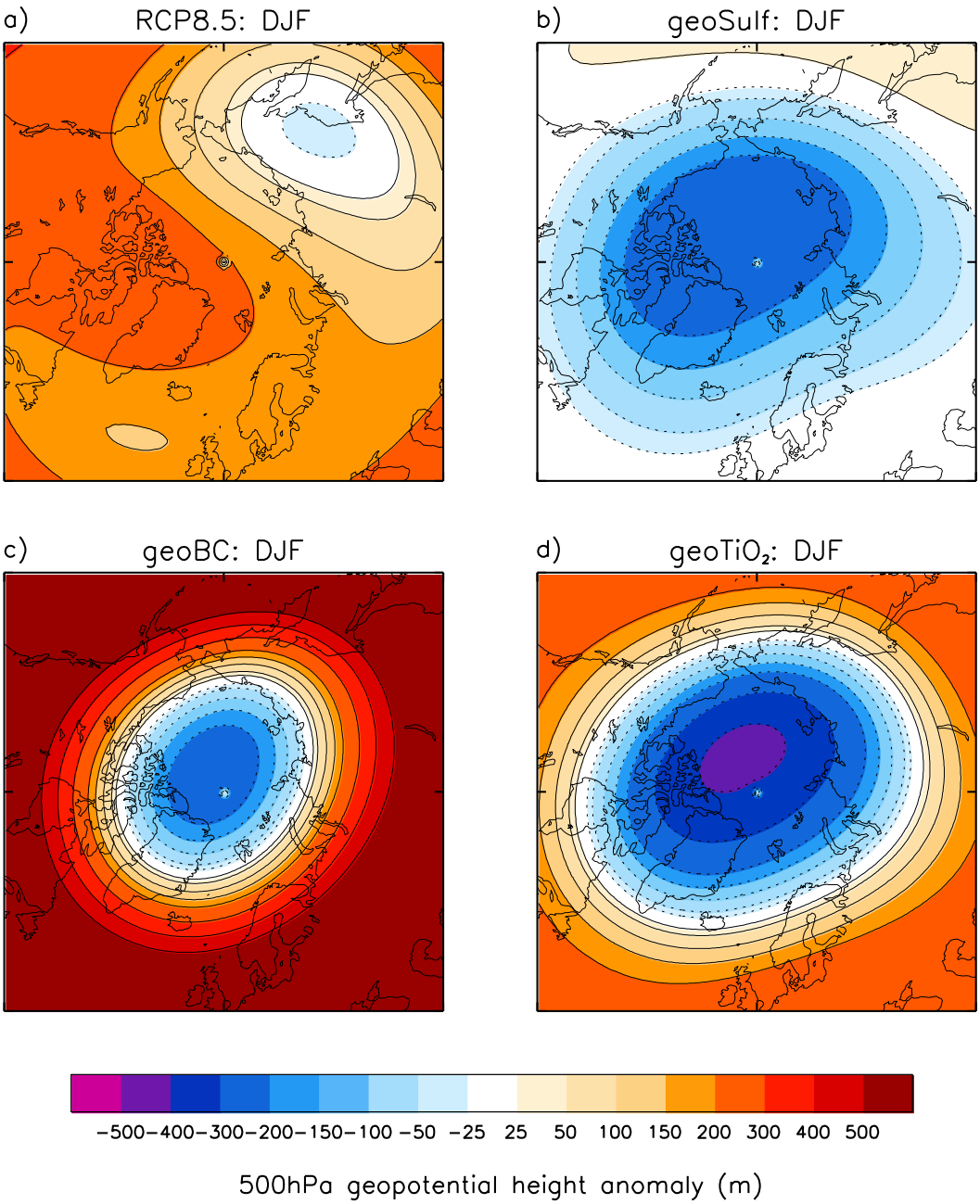

Figure 11. *DJF 50hPa geopotential height anomaly*

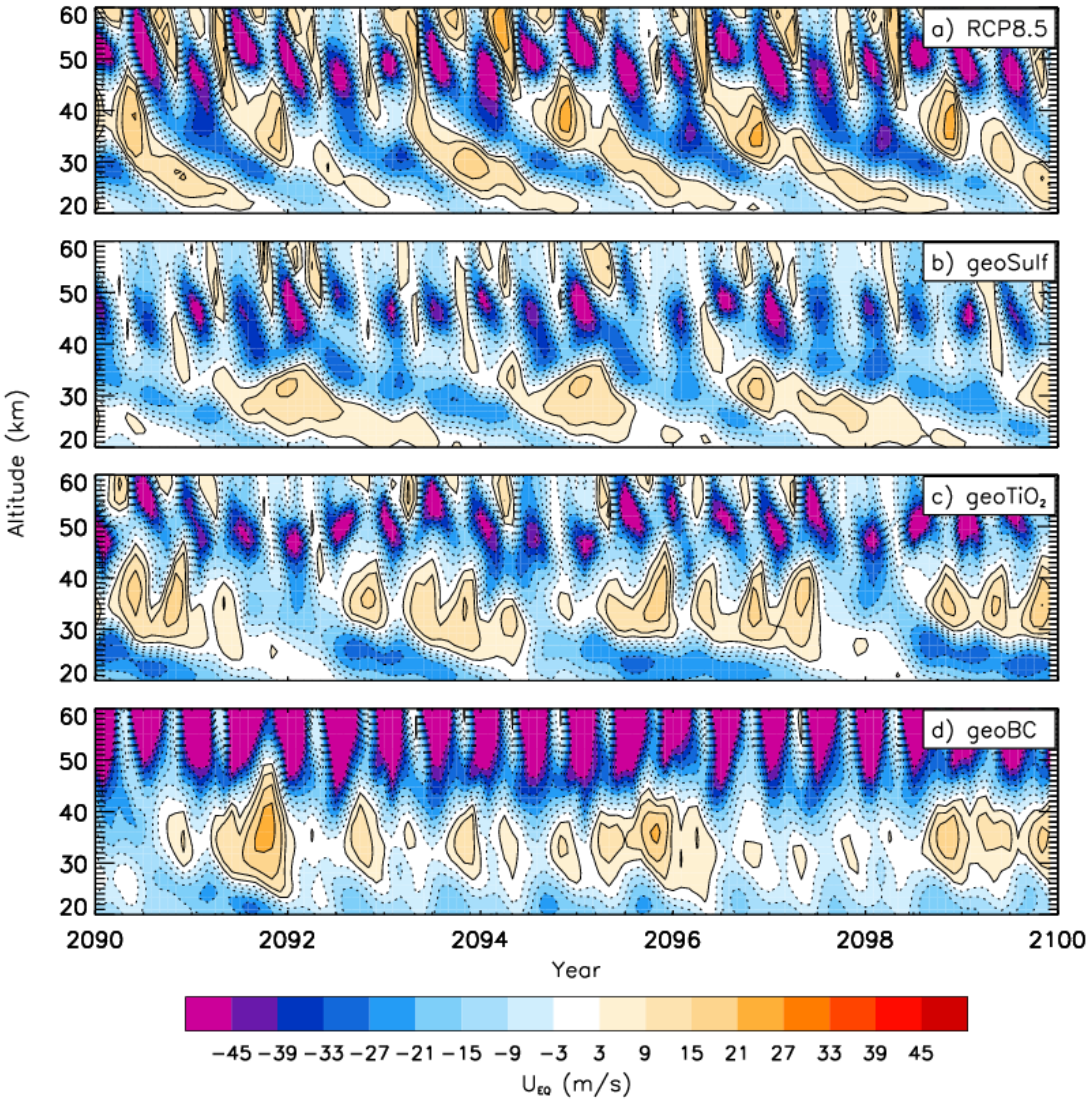

Figure 12. *Timeseries of equatorial (5°S-5°N) zonal-mean zonal wind profile*